DOWN THE RABBIT HOLE: UNRAVELING THE PATHOGENESIS OF PULMONARY CAVITATION DURING MYCOBACTERIUM TUBERCULOSIS INFECTION

by

Elizabeth A. Ihms

A dissertation submitted to Johns Hopkins University in conformity with the requirements for the degree of Doctor of Philosophy.

Baltimore, Maryland

June, 2019

Abstract

Tuberculosis infects an estimated one-third of the world's population, and is responsible for more deaths than any other single infectious agent. The continued success of *Mycobacterium tuberculosis* (MTB) in the post-antibiotic area can be attributed principally to pulmonary cavities: pathologic air spaces surrounded by scar tissue that have replaced healthy lung tissue. Cavities are the primary source of bacterial transmission during infection and contribute significantly to antibiotic resistance and treatment failure, yet the pathogenesis of cavitation is poorly understood. Proposed contributing factors include mechanical stress and enzymatic tissue destruction. To investigate these phenomena, we use a novel repetitive aerosol infection protocol in rabbits to produce a reliable model of tuberculous cavitation in which cavities are monitored by serial computed tomography. Using this model, we demonstrate that pharmacologic inhibition of collagenases does not reduce cavitation, contrary to their speculated role as drivers of cavitation. Using high-resolution 4D cavity maps to track cavity dynamics over time, we show that mechanical stress contributes significantly to

cavity formation and persistence dynamics. We also establish that central necrosis of the granuloma is a necessary precursor lesion, but is not sufficient in itself to cause cavitation. Finally, we examine the role of necrosis during infection and cavitation in C3HeB/FeJ mice – specifically, we probe the involvement of the RIP-kinase mediated programmed necrosis pathway. We demonstrate robust necroptosis activation in infected macrophages within and around granulomas in mice – the first *in vivo* demonstration of necroptosis induction during MTB infection. However, pharmacologic inhibition of RIP1 – the key decision checkpoint in the necroptosis pathway - does not alter outcomes in this model, suggesting alternative activation by one of several RIP1 bypass pathways.

In this thesis, we establish two optimized animal models for investigating the pathogenesis of cavitation, and show that these models are well-suited for screening of novel therapeutics. It is our hope that these models will be used in the future not only to further our understanding of the disease, but also to advance novel host-directed therapies to improve patient outcomes and decrease the worldwide burden of tuberculosis.

Acknowledgements

I would like to thank the following people, who had a significant influence on this thesis: William Bishai, Joseph Mankowski, Kelly Metcalf-Pate, Sanjay Jain, and Michael Urbanowski. I would also like to thank Laine Feller, Stefanie Krug, Laurene Cheung, Shichun Lun, Korin Bullin, Joshua Croteau, and Adam Wertz for their help and guidance in the laboratory.

Thank you to the following organizations and individuals for monetary and/or material support: Roche, GlaxoSmithKline, John Bertin, Igor Kramnik, National Institutes of Health (NIH) and the Howard Hughes Medical Institute (HHMI).

For their encouragement and support, I would like to thank my husband Elihu Ihms, as well as Robert and Gail Harmelink, Itzy Erin Houser, Roger Messick, and the JHU Department of Molecular and Comparative Pathobiology. Finally, thank you to Dueker, Mifkis, Otto, Igor, and Ouija – for your unconditional love and patience.

Dedication

This thesis is dedicated to the memory of William Charles Bell.

Contents

List of Tables

List of Figures

Chapter 1

Introduction

1.1 Thesis Statement

Pulmonary infection with Mycobacterium tuberculosis leads to a spectrum of pathologic changes in the lung. The most consequential of these lesions is the pulmonary cavity: an abnormal air-filled space that has replaced functional lung tissue. Despite the immense importance of cavitation in the natural history of the disease, the mechanisms underlying pulmonary cavitation are poorly understood. Elucidation of these mechanisms is critical for the development of novel host-directed therapies that will work in combination with standard antibiotics to lessen tissue destruction and reduce the spread of tuberculosis.

1.2 Motivation

Mycobacterium tuberculosis (MTB) is an ancient human pathogen. It has coevolved and traveled with human beings for millennia, peppering our history and our stories – never in the bombastic gruesome style of the Black Death, or the macabre spectre of hemorrhagic fever, but as the steady unseen hand quietly shaping the destiny of our species. This intimate relationship cultivated by MTB has garnered it a well-deserved reputation as the perfect human parasite [1].

A cure for tuberculosis first arrived in the early 1940s with the discovery of streptomycin [2]. Today, uncomplicated infections are treated with a combination of antibiotics (rifampin, isoniazid, pyrazinamide and ethambutol) for 6-9 months [2]. This antibiotic regime has greatly reduced the burden of MTB in the developed world, moving it out of the public spotlight. Meanwhile, financial and practical barriers to treatment in poorer countries allow MTB to smolder unchecked and largely unseen in much of the world [2,3]. As of 2016, the World Health Organization estimated that an astonishing one third of the world's population was latently infected with *Mycobacterium tuberculosis* [3]. MTB now competes with Human Immunodeficiency Virus (HIV) for the title of number one infectious killer [3,4].

Why does tuberculosis continue to enjoy such success in the post-antibiotic era? Antibiotic resistance is a growing problem in many species of bacteria, and MTB is no exception [3]. The long treatment times required to eliminate the infection often become burdensome to patients, causing them to prematurely terminate therapy once their clinical condition has improved [3]. Premature cessation of therapy is a major contributor to

antibiotic resistance, allowing bacteria to “sample” an antibiotic and live to tell about it. Pockets of resistant bacteria also develop within necrotic granulomas and pulmonary cavities, whose walls of fibrous scar tissue prevent movement of both antibiotics and immune cells into the microbe-rich center [5,6]. Contemporary research focuses not only on the development of novel antibiotics, but also on Host-Directed Therapies (HDTs) that work in conjunction with antibiotics to shorten treatment times and increase antibiotic penetration [7].

Perhaps the larger question is that of transmission, which has been insufficiently addressed. MTB is transmitted from person to person by the coughing of bacteria-laden aerosol droplets from deep within the lung [2]. The highest concentrations of bacteria in the infected lung are found within pulmonary cavities, which shelter them from antibiotics and the immune system [8]. The center of a cavity frequently communicates with the bronchial tree, allowing bacteria to be expelled in large numbers (Figure 1.1). Thus, cavities represent the major route of transmission for MTB. Host-directed therapies targeting cavity formation have the potential to lessen the global TB burden by reducing transmission, antibiotic resistance and treatment failure.

1.3 Historical Perspectives and Challenges

The study of tuberculosis presents a set of unique challenges not faced by other disciplines. Perhaps most obviously, *Mycobacterium tuberculosis* is a dangerous pathogen that must be handled under Bio-Safety Level 3 conditions. MTB is transmitted via aerosols, and must be kept in carefully-maintained containment facilities to prevent

its escape. Researchers undergo extensive training and wear a full suit of personal protective equipment (PPE) at all times, including a respirator. Patients are maintained in careful isolation to prevent transmission to health care workers. Working with infected animals introduces additional levels of risk, with the possibility of bites and scratches that can breach PPE. These safety considerations increase both the financial cost as well as the practical difficulty of working with MTB. Additionally, many Mycobacteria (MTB notorious among them) are extremely slow-growing, with doubling rates of approximately 24 hours in the case of MTB [2]. This corresponds to a sluggish bacterial metabolism, providing them with a measure of resistance against current antibiotics which target actively growing organisms [2]. In patients, it takes 6-9 months of continuous multimodal antibiotic therapy to achieve sterilization [2]. Both *in vivo* and *in vitro*, this translates into slow-moving experiments with long periods of waiting. A simple mouse monotherapy experiment (such as that described in Chapter 4) can be performed in approximately 12 weeks. More complicated animal studies involving combination antibiotic therapy and relapse may take up to a year to complete, and latency studies are often performed over the course of several years.

Yet ironically, perhaps the greatest hindrance to TB research came in the form of Streptomycin, which so rapidly and efficiently removed Mycobacteria from the lungs and minds of wealthy westerners that it quickly condemned TB to the ranks of forgotten third world diseases. Research efforts declined precipitously in the second half of the 20th century following a steady decline in public funding. These were the “dark ages” of TB research which only came to an end when the 1980’s brought the Human

Immunodeficiency Virus (HIV) to the western world. MTB – far from eradicated - had been hiding quietly in America for the intervening years, maintained in conditions of poverty and overcrowding which cause a natural aversion of the attention. HIV generated a fresh pool of immunodeficient adults, setting the perfect stage for MTB to make its comeback.

Large gaps still exist in our basic understanding of the bacterium and the disease it causes, with much of our foundational knowledge built on work from the early 20th century. Relying on literature of this period introduces additional obstacles as one attempts to decrypt the meaning of imprecise and archaic terms in the context of a modern understanding of molecular pathology. Particular difficulty comes when trying to accurately apply these terms in a discussion on TB immunology. For example, "latency" is described as a phenomenon whereby tubercle bacilli enter a dormant state in the host, reactivating years or even decades later [9]. Yet clinically, latency is merely defined by a positive immune response to tuberculin proteins (whether by Manteaux or Interferon Gamma Release Assay) – tests which merely measure exposure to mycobacteria and are unable to discriminate between current and resolved infections, or even between TB infected and BCG-vaccinated individuals [9]. Efforts to integrate historical and modern data under united terminology are ongoing [10].

Access to patient samples was unparalleled in the first half of the 20th century, and carefully documented observations by pathologists such as Rich and Canetti are invaluable for a constructing a true picture of TB pathogenesis [11,12]. However, when one considers the natural course and potential outcomes of tuberculosis, it becomes clear that

such autopsy data segregates neatly into two patient populations: (A) Those with fulminant tuberculosis who died of their disease, and (B) those with latent or resolved tuberculosis who died of something else entirely. Thus, the inherently biased nature of post-mortem patient data leaves us with an incomplete picture, and emphasizes the critical importance of developing animal models in which all stages of the disease can be replicated under controlled conditions.

1.4 Animal Models of Tuberculous Cavitation

Primates. Historically, research into the mechanisms of cavitation has been hindered by a lack of animal models that reliably reproduce the pathology of the disease as seen in humans [13]. The human response to MTB infection is remarkable for its extreme heterogeneity, both between and within patients. Disease manifestations are highly variable, and a diverse spectrum of lesions is often observed within the lungs of a single patient [12,14]. Because of this extreme variability, no single animal model recapitulates all aspects of the human disease, with the possible exception of our closest relatives, nonhuman primates (NHPs). As in much of biomedical research, NHPs could perhaps be considered the gold standard model of pulmonary tuberculosis, although significant obstacles limit their usefulness as a model of TB cavitation. Similar to their human counterparts, NHPs develop cavities sporadically and at a low frequency, though their large size permits advanced imaging techniques such as CT and MRI. Although the relatively longer lifespan of primates facilitates collection of valuable cohort data over time, the low numbers of animals used often limits the generalizability of such studies.

Finally, practical and financial considerations such as animal availability, handling, study design and BSL3 housing are major limiting factors in the use of primates. Because of these obstacles, no systemic studies of cavitation have been undertaken in primate models to date.

Rabbits. The rabbit has been used to model several aspects of TB disease, and gained scientific popularity in the 1950s with Lurie's characterization of genetically susceptible and resistant inbred rabbit populations [15]. Cavitation was documented sporadically in these early rabbit models, and only after long periods (6-10 months) [16]. Lurie's inbred lines were unfortunately not maintained, and modern rabbit studies use outbred rabbits such as the New Zealand White, which have a high natural resistance to MTB. *Mycobacterium bovis* is thus frequently used to model tuberculosis in rabbits due to its relatively higher virulence in this species. Unlike MTB, *M. bovis* results in fulminant pulmonary disease in rabbits and therefore a more rapid onset of cavitation [17]. Using *M. bovis* in outbred rabbits, Dannenberg advanced the work of Lurie by characterizing the role of cell-mediated immunity (CMI) and delayed type hypersensitivity (DTH) in cavity generation [18], confirming cavitation as an immune-mediated event. However, *M. bovis* also frequently results in disseminated disease in multiple species including rabbits [19,20] – a phenomenon not typically seen in human TB except in cases of altered immune function [12]. As cavity generation in TB patients is correlated with immune status [21], the utility of the aerosol *M. bovis* model for interrogating the pathogenesis of cavity generation is uncertain. Kübler further modified this model by pre-sensitizing animals with intradermal heat-killed *M. bovis* prior to bronchoscopic delivery of live *M. bovis*

into a single lung lobe, reliably producing a single large cavity at the site of inoculation [22]. The reproducibility and application of advanced imaging techniques makes this model valuable for investigating the local environment and life cycle of pulmonary cavities. The Kübler model greatly advanced our understanding of pulmonary matrix degradation during infection [23,24], but has been criticized for its highly artificial method of cavity induction. Chapter 2 introduces a novel method of repetitive aerosol MTB infection that reliably induces a high frequency of cavitation in rabbits [25]. By utilizing aerosolized *M. tuberculosis* rather than *M. bovis*, rabbits more faithfully reproduce the human disease, generating a heterogeneous spectrum of pulmonary lesions with infrequent extrapulmonary spread. In Chapter 3, we use serial high resolution imaging in this model to interrogate the dynamics of cavity formation over the course of infection. A major disadvantage of any rabbit model is the limited availability of immunologic reagents, as a preponderance of commercial antibodies are produced in rabbits.

Mice. Known prerequisites for cavitation include the induction of a strong DTH response [18] and the onset of necrosis [26] – two characteristics that are lacking in mouse models of TB infection in commonly used mouse strains C57BL/6 and BALB/c. Upon challenge with MTB, these mice develop solid cellular granulomas that lack necrosis or caseation, making them unsuitable models of human TB pathology [27]. The recent characterization of the C3HeB/FeJ mouse – a general purpose immunocompetent strain that responds to TB infection by forming large caseating granulomas [28] – has brought mice once again to the forefront of tuberculosis research. In further support of the close association between necrosis and cavitation, these mice also have a high incidence of

pulmonary cavitation [29], making them the first rodent model of cavitation. An obvious advantage of this model is that is highly amenable to genetic manipulations – a factor already being exploited by several investigators to uncover genetic determinants of host necrosis during TB infection [30–32]. In Chapter 4, we use the C3HeB/FeJ mouse to investigate the molecular determinants of host necrosis and the involvement of programmed cell death pathways.

1.5 Comparative Pathology of Cavitation

Spatial. The most obvious facts are the ones most often taken for granted. It often goes without saying that cavitation is a phenomenon unique to the lung. Yet this high locational selectivity reveals important insights about the pathogenesis of cavity formation that are infrequently discussed. Unlike other solid organs, the lung is constantly being subjected to fluctuating pressures and tension forces within the thoracic cavity. Constant negative pressure in the pleural space maintains the lungs in an inflated state, similar to a balloon in a bell jar [33]. During inspiration, expansion of the chest wall and relaxation of the diaphragm cause this negative pressure to increase, pulling the lungs open and allowing air to flow in passively [33]. This repetitive mechanical stress is not experienced by other internal organs, and contributes significantly to cavity formation [26]. Healthy lung tissue contains a mixture of collagen and elastin, which provide structural integrity and elastic recoil, respectively [19]. In diseased lung tissue, this matrix has been replaced by fibrovascular scar tissue which has reduced tensile strength and very little elasticity [19]. In chapter 3, we examine the distribution and behavior of pulmonary cavities

in rabbits, and present additional evidence that mechanical action promotes cavity formation by disrupting the walls of necrotic pulmonary granulomas.

Structural. Although frequently thought of as a characteristic finding, pulmonary cavities are by no means pathognomonic for tuberculosis. A diverse set of diseases – ranging from other infectious diseases to primary lung cancers – may result in pulmonary cavities, though of these MTB has the highest incidence [21]. Despite their etiologic diversity, a survey of cavitary diseases for commonalities reveals that cavitary lesions share certain structural requirements. First, the interior of the lesion must be soft or liquefied, composed of necrotic debris which can escape into adjacent airways. Secondly, the exterior of the lesion must be structurally solid, so that it remains behind when the necrotic center is removed to form the wall of the cavity. Central necrosis often occurs in aggressive lung tumors (such as squamous cell carcinoma) as they outgrow their blood supply. As the tumor enlarges, necrotic debris drains into eroded airways, leaving behind an air-filled cavity with a wall composed of living tumor cells. A similar process occurs in subacute to chronic bacterial and fungal pneumonias. In the case of *Klebsiella pneumoniae*, which causes a subacute to chronic necrotizing pneumonia, large pus-filled abscesses are formed in the lung, which drain to leave behind a wall of scar tissue and inflammatory debris [21]. Chronicity seems to play an important role in determining whether or not a cavity will form by virtue of how much scar tissue has accumulated around the necrotic regions, as more acute necrotizing process are less likely to cavitate [21].

Immunologic. In contrast to the granuloma, relatively little is known about the regional immunology of the cavity. CD4+ T cells were implicated as critical participants in the cavitation process when it was noticed that the incidence of cavitation is inversely correlated with declining CD4+ counts in HIV+ patients – not only for tuberculosis, but also for other common opportunistic infections [21]. In these cases, your risk of cavitation actually decreases as your risk of infection and severe disease increases. An explanation for this can be gleaned from serum cytokine abnormalities in patients with cavitary disease. Interleukin-4 (IL-4) increases in patients with advanced disease [2] and is also correlated with the extent of cavitation [34,35]. (Although importantly, we demonstrate in Chapter 3 that these two conditions are not necessarily correlated). Protective immunity to tuberculosis depends on a strong pro-inflammatory Th1 polarized response with robust production of IFNγ and TNFα. Conversely, failed immunity is associated with Th2 polarization and a shift to IL-4 and TGFβ production, creating a more tolerigenic environment that favors bacterial proliferation and drives immunopathology [2]. These systemic changes are similarly reflected at the level of the individual lesions, with each granuloma harboring a distinct Th1-Th2 balance [36,37]. Cavitary lesions are characterized by interior depletion of lymphocytes and high levels of bacterial replication. In this sense, a cavity represents a regional instance of failed immunity, although much remains to be learned about how this failure occurs [38].

Enzymatic. Multiple proteolytic enzymes have been implicated in the pathogenesis of tuberculous cavitation by their spatial upregulation in and surrounding cavities [24,39]. Once unleashed, these collagenases and cathepsins initiate proteolytic cascades with high

destructive potential, making them attractive scapegoats in the pulmonary destruction that accompanies cavitation. However, teasing apart their role as either active drivers of cavitation or secondary responders to tissue damage has not yet been possible [25]. As we discuss in the following two chapters, it is likely that the truth lies somewhere between the two extremes.

Figures

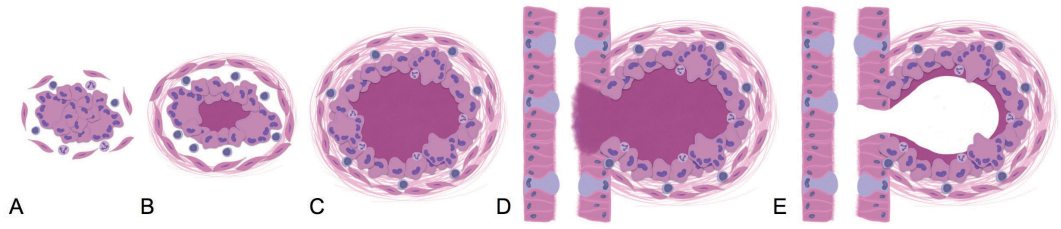

Figure 1.1: The current model of cavity formation involves granuloma liquefaction and airway invasion. (A) Granuloma formation begins with an aggregate of activated macrophages, multinucleated giant cells, lymphocytes and neutrophils. (B) As the lesion enlarges, the center may undergo progressive necrosis, liquefaction and inspissation, resulting in the characteristic “caseous" appearance. (C) Formation of a variably thick outer capsule of fibroblasts and collagen occurs with chronicity. (D) If a large necrotic lesion arises in proximity to an airway, proteolytic enzymes in the necrotic center may lead to erosion into the bronchial tree. (E) Expulsion of necrotic contents into the airway leave behinds a thick-walled air-filled cavity which freely communicates with the respiratory tree.

Chapter 2

Repetitive Aerosol Exposure Promotes Cavitary Tuberculosis and Enables Screening of Host-Directed Therapies

2.1 Authorship note

This chapter represents the combined efforts of Drs. Elizabeth Ihms and Michael Urbanowski. The double-exposure experiments were conceptualized and designed by MEU, and performed with assistance from EAI. For the MMP inhibition studies, all animal studies were jointly designed and performed by MEU and EAI. LC/MS-MS work was performed by MEU with help from KB and SL, and histopathology quantification was performed by EAI.

2.2 Background

Tuberculosis (TB) is a major cause of morbidity and mortality worldwide, with an estimated 10.4 million new cases of TB and 1.4 million deaths occurring in 2015 [1]. Individuals with active disease develop a spectrum of gross lesions including diffuse pulmonary inflammation, organized granulomas or "tubercles," caseous granulomas, and cavities. The most consequential of these lesions is the pulmonary cavity. While not specific to TB, cavities are the greatest risk factor for transmission of tuberculosis bacilli [2–5]. Cavitary TB is also more difficult to treat than noncavitary disease, and is associated with the emergence of drug resistant infections [6]. For patients with cavities who have been cured of TB, their cavities often remain, creating a niche for opportunistic infections [7]. Cavitary lesions that do resolve are associated with fibrotic scarring and reduced long-term pulmonary function [8,9].

A perfect storm of pathologic landscapes coincides within cavities to drive transmission and reduce the likelihood of treatment success. The interior surface of the cavity represents a well-oxygenated and immune privileged site that permits high levels of extracellular bacterial proliferation [6,10]. Moreover, cavities frequently communicate with adjacent conducting airways, providing a perfect physical conduit for aerosolization and transmission [11]. Finally, scar tissue and widespread necrosis within the cavity wall reduce the penetration of chemotherapeutic drugs, promoting antibacterial resistance [12–15]. Despite the importance of cavities to the natural history of TB, the mechanism of cavity formation in TB remains unclear. Histologically, cavities are thought to arise from necrotic granulomas, whose centers are both devoid of extracellular matrix. Pulmonary

extracellular matrix is composed primarily of collagen and elastin, which provide mechanical support to the lung while maintaining compliance and elasticity. The expression of collagenases leads to caseation, suggesting that collagen depletion may be an early mechanistic driver of cavitation [16–18]. Indeed, increased expression of collagenases is also associated with cavity formation in both animal models and patients with TB [19, 20].

A major limitation to studying cavitary tuberculosis has been the lack of reproducible animal models. Mice and guinea pigs rarely develop cavities, whereas they do occur in nonhuman primate and rabbit models [21–23]. Previous studies in rabbits have employed pre-sensitization with heat-killed tubercle bacilli followed by a high-dose aerosol, transthoracic, or intrabronchial challenge [24–26]. While these methods result in cavitation in some animals, they also generate extensive regional pneumonia, making it difficult to monitor granuloma formation, necrosis, and progression to cavity formation.

Here we describe a novel model for cavitary TB based on repeated aerosol exposure in rabbits. This model reliably generates multiple cavitary foci in 60%–80% of study animals in a short period of time. Compared with single exposures of the same total bacterial burden, repetitive exposure generates more advanced disease and more cavitary foci, suggesting that repetitive exposure to aerosolized bacilli may be an important determinant of disease severity in high-incidence settings. Recently, the number of exposures experienced by newly infected TB patients was reported as a risk factor for disease progression [27]. This model reliably develops human-like pulmonary cavities where matrix depletion is a major pathologic feature of cavity development. Finally, we

have applied this model to screen cipemastat, a potent inhibitor of matrix metalloproteinase-1 (MMP-1), as a potential host-directed therapy to limit the extent of tuberculous cavitation [28,29].

2.3 Methods

Infection of Rabbits. All procedures involving live animals were conducted in accordance with protocols approved by the Institutional Animal Care and Use Committee at the Johns Hopkins University School of Medicine. Adult female New Zealand White rabbits (2.5–3.5 kg) were purchased from Robinson Services (Mocksville, North Carolina) and individually housed in a Biosafety Level 3 facility without cross-ventilation. Rabbits were infected in a Madison aerosol droplet generation chamber (College of Engineering Shops, University of Wisconsin, Madison). The aerosol inoculum for the chamber was prepared by dilution of log-phase bacterial culture of M. tuberculosis H37Rv to the appropriate optical density (OD) for each experimental group.

Cipemastat Dosing. Cipemastat was obtained from the Roche Corporation (Basel, Switzerland), and the identity of the compound was confirmed by liquid chromatography and tandem mass spectrometry (LC/MS-MS). Rabbits in the treatment group were given 100 mg/kg cipemastat orally by body weight using PediaSure as a vehicle. The concentration of cipemastat in the vehicle was 100 mg/mL. Cipemastat treatment and vehicle shams were administered daily during study weeks 5–11.

Pharmacokinetic Analysis of Cipemastat in Plasma. Three rabbits were given a single 100 mg/kg oral dose of cipemastat. Peripheral blood samples were collected every

30 minutes, then at 4, 6, 8, 12, and 24 hours. Experimental samples were analyzed in tandem with a standard curve prepared in untreated rabbit plasma. Plasma concentrations of cipemastat were detected and quantified by liquid chromatography–tandem mass spectrometry (AB SCIEX QTRAP 5500). Liquid chromatography was carried out by reverse-phase gradient elution between 90% mobile phase A (0.1% formic acid in water) and 95% mobile phase B (100% acetonitrile) over 2 minutes on a ZORBAX Eclipse Plus C18 column (2.1 × 50 mm, 3.5 μm, Agilent Technologies). Selected ion monitoring of the cipemastat parent ion at m/z 437.2 identified daughter ions at m/z 262.2 and 404.3. These transitions were supported by predicted masses in a cipemastat fragmentation map and agree with transitions identified by Hopfgartner et al [30]. Cipemastat concentration in eluate was measured as the area under the curve for mass transition peaks. Analysis was conducted using Analyst (SCIEX) and companion software MultiQuant (SCIEX). Pharmacokinetic (PK) analysis of total drug exposure over time (AUC0-24), half-life (T1/2), concentration maximum (Cmax), and time of concentration maximum (Tmax) were calculated using 2-compartment first-order PK analysis with WinNonlin software (version 7.0, Pharsight Corp).

Computed Tomography. Rabbits were sedated with intramuscular injections of xylazine (3 mg/kg), ketamine (25 mg/kg) and acepromazine (1 mg) prior to bronchoscopically–assisted intubation with a 3.5 mm endotracheal tube (Teleflex Medical, Research Triangle Park, NC). Following intubation, animals were imaged using a CereTom 8-slice clinical computed tomography (CT) scanner with a 32.5-cm bore diameter (NeuroLogica, Boston, Massachusetts). To achieve reconstructions in the

absence of motion artifact, breath-holding was performed during CT scans as previously described by Kübler [31]. Briefly, anesthetized rabbits were maintained at physiologic peak inspiration for approximately 15 seconds during image acquisition.

Identification of Cavities From CT Reconstructions. Raw CT scan data was compiled into DICOM files using Loening Amide (Version 0.9.0). CT reconstructions were analyzed using VivoQuant software (Invicro). Pulmonary cavities were radiologically identified from CT scan reconstructions as a contiguous set of volume elements (voxels) with densities close to air (–1000 to 910 Hounsfield units [HU]) and encapsulated by consolidation, defined as a continuous region of voxels with densities similar to water (–725 to 1000 HU). This radiological definition was consistent with the consensus definition for cavities advanced by Gadkowski and Stout [2]. Contiguous airspace and consolidation regions were selected by connected thresholding in the density range for each landmark.

Necropsy and Histopathology. IM sedation was performed as previously described, after which animals were euthanized with 2-3cc IV pentobarbital solution in the marginal ear vein. Gross images of the lungs were obtained using a Nikon D3200 digital camera and a Nikon NIKKOR lens and analyzed with ImageJ to identify the areas of visually diseased lung as a fraction of the total area of splayed lung [32]. Lungs were then gently infused with intratracheal 10% neutral buffered formalin prior to fixation for 48 hours. Transverse lung slices were processed for paraffin embedding and histologic sectioning. Serial 5 μm sections were stained using hematoxylin and eosin, Masson's trichrome stain, or acid-fast stain. Image capture for semiquantitative trichrome quantification was

performed on a Nikon Eclipse 90i microscope with attached Nikon DS-Ri1 color camera, and analyzed using NIS Elements Advanced Research software (Nikon Instruments, Melville, New York). Regions of interest (ROI) included the full thickness of the cavity wall while excluding necrotic debris and air space at the cavity interior. Positive staining was calculated as a percentage of the total ROI.

Substrate Cleavage Assay. Recombinant human MMP-1 (BioVision, Milpitas, California) was added to a solution of type I collagen (Thermo Fisher Scientific, Waltham, Massachusetts) in phosphate-buffered saline at a molar ratio of 1:5. One hundred microliters of Novex Zymogram 1X Developing Buffer (Thermo Fisher Scientific, Waltham, Massachusetts) with or without 1 μg cipemastat was added to this solution prior to incubation at 37°C for 24 hours. At 24 hours, an equal volume of ethylenediaminetetraacetic acid (EDTA) was added to stop the cleavage reaction, and the products were briefly boiled and subjected to sodium dodecyl sulfate–polyacrylamide gel electrophoresis on a Mini-Protean TGX precast gel (Bio-Rad, Hercules, California).

2.4 Results

Repetitive aerosol exposure to M. tuberculosis causes a high frequency of cavitation in a rabbit model. Sensitization of animals by injection of heat-killed mycobacteria prior to infection increases the frequency and severity of cavitation in rabbit models [26,31]. We reasoned that multiple aerosol challenges with virulent M. tuberculosis would provide a robust and sustained immune-sensitizing effect by simultaneously antagonizing both innate and adaptive defenses, thereby increasing cavity

generation. To test this hypothesis, we infected rabbits with M. tuberculosis using two different exposure patterns. For our studies, we defined exposure as the product of the bacterial concentration in the aerosol inoculum and the total time spent in the aerosol chamber. One group of rabbits received five aerosol challenges with M. tuberculosis at an optical density (OD600) of 0.05 over a 2-week period. A second group of rabbits received a single aerosol challenge with M. tuberculosis at an OD600 of 0.25, five times that of the repetitive exposure (Figure 2.1A). Each challenge corresponded to a bacterial implantation of approximately 400 colony-forming units (CFUs) per exposure in the OD 0.05 group, and 2200 CFUs per exposure in the OD 0.25 group (Figure 2.2). We established that the cumulative exposure was the same for both groups by measuring the CFUs in the aerosol inoculum (Figure 2.1A). To confirm that concentrations of bacilli are linearly correlated with the OD of the aerosol inoculum, we performed a titration assay to compare the inoculum OD with the day one implantation of bacteria in the lungs, and showed a linear correlation in the OD range used in these experiments (Figure 2.2). Our data indicate that it is likely that repetitive exposure rabbits were inoculated on every occasion of exposure, as bacteria were reliably recovered from the lungs of all animals in the lowest exposure group (Figure 2.2).

Cavity development was monitored using serial computed tomography. 75% (3/4) of the animals in the repetitive exposure group developed at least one cavity, vs. 25% (1/4) of the animals in the single exposure group (Figure 2.1B). Of the animals that cavitated, those in the repetitive exposure group developed more cavities per animal than those in the single exposure group (Figure 2.1C). By 10 weeks post-infection, animals in the

repetitive aerosol group experienced worse lung disease than those in the single exposure group (Figure 2.1D and Figure 2.3). These data demonstrate that repetitive exposure results in an increase in the severity of disease as well as the frequency and severity of cavitation.

Cavities from repetitive exposure form quickly, show dynamic behavior, and often persist for many weeks. To study the dynamics of cavity formation generated by repetitive exposure to M. tuberculosis, eight rabbits were infected with M. tuberculosis using the repetitive exposure protocol and monitored by serial CT scans. The overall frequency of cavitation in this study was 87% (7/8), further supporting our previous observations with the repetitive exposure method (Figure 2.4A). The greatest increase in the frequency of cavitation occurred between weeks 6 and 8, during which time the frequency of cavitation increased from 11% (1/8) at week 6 to 50% (4/8) at week 8 (Figure 2.4A). Between weeks 8 and 16, the frequency of cavitation increased modestly to 63% (5/8), but was also marked by the occasional resolution of existing cavities and the generation of new cavities. Three-dimensional CT reconstructions of the lungs were analyzed to evaluate changes in cavity morphology over time. From this analysis, we identified 3 patterns of change in cavity morphology: (1) growth (Figure 2.4B and 2.4C, examples 1, 2, and 3); (2) shrinkage (Figure 2.4B and 2.4C, examples 2 and 3); and (3) resolution (Figure 2.4B and 2.4C, example 4). Together, these data demonstrate that the peak of cavitation occurs between 6 and 8 weeks after initial aerosol exposure, and that cavities are persistent and dynamic structures.

Central necrosis and matrix depletion are prerequisites for cavitation. A large body of historic literature, in addition to our own observations, demonstrates that tuberculous cavities arise from necrotic granulomas. To further characterize cavities generated by repetitive exposure to M. tuberculosis, we investigated whether the pathologic phenotype of lung destruction was similar to that observed in the human disease. Histologically, lungs from rabbits infected by repetitive exposure display many of the microscopic findings described in patient autopsy reports (Figure 2.5A) [10,21,33,34]. These hallmarks include granulomas, necrotic granulomas, and cavities. Histologic observations from the repetitive exposure model demonstrate similar cytoarchitecture between necrotic granulomas and cavities, further supporting a close relationship between these lesions (Figures 2.5A, 2.5B, and 2.6C). The cavities generated by repetitive exposure were marked by large proliferations of acid-fast bacteria along their inner surface and an outer fibrotic wall (Figure 2.5B). Because our investigations are predicated on the pathologic observation that matrix depletion predisposes to cavitation, we also confirmed that collagen depletion was a hallmark of cavitary lesions from repetitive exposure (Figure 2.6). These observations show that repetitive aerosol exposure in rabbits generates a spectrum of histologic lesions commonly observed in human TB pathology, and validates the model for investigation of pathologic matrix depletion.

The collagenase cipemastat is orally bioavailable in rabbits and reaches therapeutic concentrations in peripheral blood. Cipemastat is a potent inhibitor of MMP-1 and was originally developed by the Roche Corporation as an antiarthritis agent [28,29]. We confirmed that cipemastat inhibits MMP-1 *in* vitro (Figure 2.7) and has no

intrinsic antimycobacterial activity (Table 2.1). To confirm that cipemastat is orally bioavailable in rabbits and had suitable kinetics for a daily dosing regimen, we conducted a 3-rabbit pharmacokinetic study. Rabbits were given a single 100 mg/kg oral dose of cipemastat, a dose previously shown to be within the tolerability and efficacy range in human and animal studies [35,36]. Peripheral blood samples were taken at regular intervals over a 24 hour period, and analyzed by LC/MS-MS. The results of the PK study showed an AUC 0-24hr of 21.79 h × μg/mL (49.9 μM × h), consistent with previously published oral dosing studies (Table 2.2, Figure 2.8) [35,36]. Importantly, we found that the plasma concentration remained above the published half maximal inhibitory concentration (IC50) of 26 ng/mL (60 nM) for 22 of 24 hours following a single oral dose (Table 2.2 and Figure 2.8) [28]. These results demonstrate that cipemastat is orally bioavailable in rabbits and confirms that a daily dosing regimen is sufficient to maintain plasma concentrations above the IC50.

Concentration		128	64	32	16	8	4	2	1	0.5	0.25
cipemastat-1	% inhibition	-5.61	-6.06	-2.32	-1.69	-4.30	-5.38	1.34	-5.84	-1.33	-8.56
cipemastat-1	raw counts	57234	57491	55483	55099	56514	57133	53420	57374	54842	58848
cipemastat-2	% inhibition	1.91	-1.78	3.10	-0.15	0.93	3.20	-0.99	-3.66	-0.04	-0.94
cipemastat-2	raw counts	53132	55071	52479	54228	53634	52415	54664	56123	54196	54733
cipemastat-3	% inhibition	-3.85	-1.71	-1.33	4.02	2.77	5.75	9.50	-0.69	2.51	6.84
cipemastat-3	raw counts	56208	55049	54836	52010	52623	51006	48971	54460	52777	50408
Concentration		1.28	0.6	0.32	0.16	0.08	0.04	0.02	0.01	0.005	0
isoniazid	% inhibition	96.62	95.96	91.98	88.79	86.93	86.14	83.78	80.32	74.18	-3.01
	raw counts	8742	6734	6906	7048	7561	7703	8814	10668	13971	55736

Table 2.1: Results of Alamar Blue assay showing *M. tuberculosis* H37Rv growth in the presence of varying concentrations of cipemistat and isoniazid.

	AUC_{0-24} (hr*µg/mL)	C_{max} (µg/mL)	T_{max} (hr)	$T_{1/2}$ (hr)
cipemastat	19.92 (16.42-23.44)	3.02 (1.99-4.44)	2.47 (1.98-3.07)	1.87 (1.22-2.23)

Table 2.2: Pharmacokinetic data for cipemastat in rabbit plasma following bolus dosing.

Cipemastat monotherapy does not protect against extensive lung destruction or cavitation. MMP-1 transcripts accumulate within regions of M. tuberculosis–induced lung damage, suggesting that MMP-1 activity may drive tissue destruction during infection [19]. We thus hypothesized that inhibition of MMP-1 would mitigate cavity development (Figure 2.5C). We randomized 18 rabbits into an 8-rabbit vehicle group and a 10-rabbit cipemastat group. Animals in the cipemastat group received 100 mg/kg of cipemastat orally in PediaSure from weeks 5 through 11 post infection. This treatment window includes the weeks preceding the predicted onset of cavitation during which matrix depletion is occurring in lesions (Figure 2.10). Breath-hold CT scans were performed on all study animals at weeks 5, 7, 9, 11 and 14. These CT scans revealed no significant difference in the number or size of cavities between the control and treatment groups throughout the study, though cipemastat-treated animals showed a trend towards more severe cavitary disease (Figure 2.10 and 2.11).

Collagen content of cavity walls is unchanged by cipemastat treatment. Tuberculosis lung lesions are often encircled by a fibrotic wall [21]. This pathologic matrix deposition is also a feature of rabbits modeling cavitary TB (Figures 2.5B and 2.10D). As cipemastat inhibits the activity of collagenases, we predicted that cipemastat administration would increase the collagen content around TB lesions. Formalin-fixed paraffin-embedded 5um lung sections were stained with Masson's trichrome for collagen.

Hue-thresholding was then used to quantify the amount of collagen within and around lesions. Surprisingly, there was no difference in the amount of collagen deposition between treated and control animals, suggesting that cipemastat treatment does not alter the course of pathologic collagen deposition around cavities in the rabbit model (Figure 2.10D).

2.5 Discussion

We have developed a novel model for cavitary TB based on repeated aerosol exposure to virulent M. tuberculosis. Our data show that repetitive exposure over a 2-week period produces more advanced disease and more cavities than a single exposure, even when adjusting the concentrations of bacteria to provide the same total exposure between groups. This finding suggests a link between repetitive exposure and TB exacerbation and is further supported by recent epidemiological evidence that multiple exposures to infected contacts increases the risk of TB progression [27]. An association between repetitive exposure and severe TB may have important implications for epidemiology and infection control in high-incidence countries [37]. Our experiments did not evaluate the mechanism of repetitive exposure–related disease exacerbation; however, it is likely that the driver of more severe disease in repeatedly exposed animals is repeated priming of cell-mediated immunity. Repetitive exposure may cause a cascading set of T-cell priming and expansion events that disproportionately exacerbate the immune response against M. tuberculosis antigen in the lung [38]. Modeling cavitary

TB by repetitive aerosol exposure also models a spectrum of human lesions and pathologic matrix depletion associated with caseous and cavitary pulmonary TB [39].

We took advantage of this model to screen cipemastat, a potent inhibitor of MMP-1, as an potential host-directed therapy to decrease cavitation [28]. Our study was supported by a molecular phenotype in which MMP-1 expression increased around tuberculous lesions with matrix destruction [19]. In these experiments, we administered cipemastat for 4 weeks preceding the development of caseous and cavitary lesions in the repetitive aerosol model. However, treated animals did not show a reduction in cavitation or disease severity. As part of our investigations, we confirmed that the plasma concentrations of cipemastat were well above the IC50 during the 24-hour dosing cycle. We did not sample the concentration of cipemastat in TB lesions, so it is possible that cipemastat did not reach inhibitory concentrations within granulomas undergoing matrix destruction. Furthermore, MMP activity may be highly localized in pericellular niches or otherwise sequestered from chemotherapeutics [40]. Alternatively, MMP-1 may act in conjunction with other extracellular collagenases to drive matrix depletion, reflecting redundancy in the proteolytic cascade. Finally, it is possible that MMP-1 is not a mediator of matrix depletion and cavitation. The increased expression of MMP-1 at TB lesions may be purely associative or indicate another role for MMP-1 in the pathobiology of TB. Our results demonstrate an entirely new model system to study tuberculous cavities. We show that repetitive exposure to aerosolized M. tuberculosis produces a pathologically relevant phenotype for screening preclinical agents toward the prevention and treatment of cavity formation.

Figures

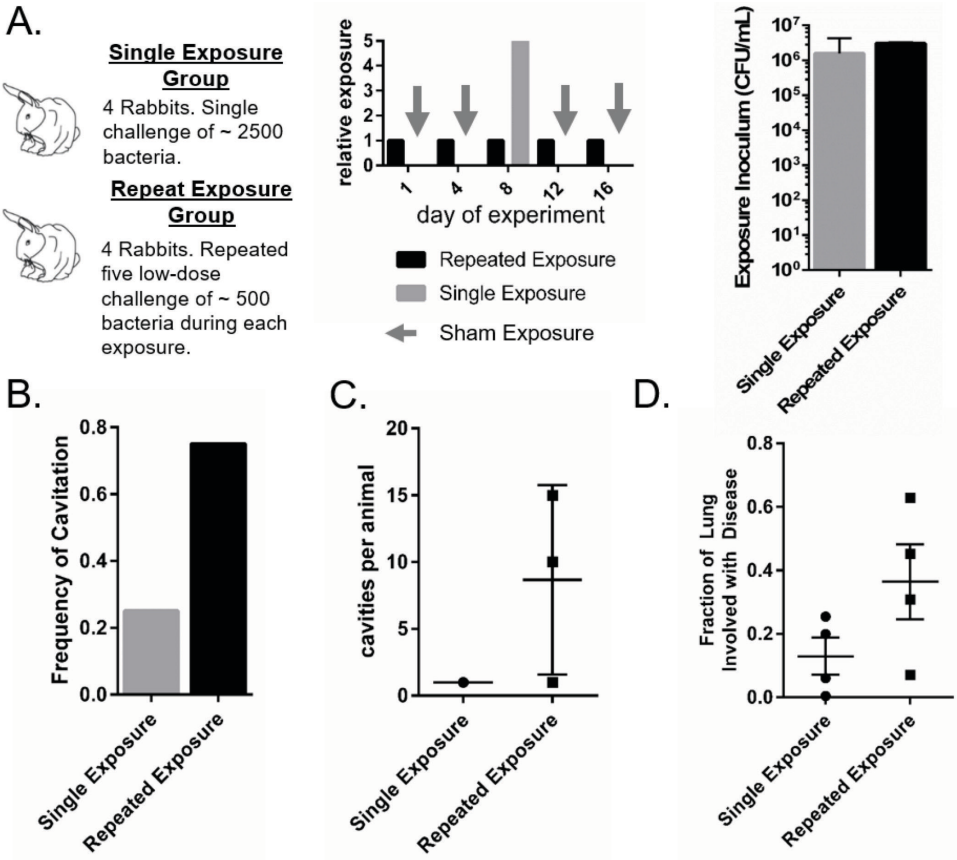

Figure 2.1: Infection parameters and disease patterns for rabbits challenged in the single exposure group and the repeated exposure group.
(A) Experimental exposure conditions and timing. Single exposure group rabbits received a single implantation with approximately 2500 bacteria on day 8 and sham exposures to aerosolized PBS on days 1, 4, 12 and 16. Repeated exposure group rabbits received five repeated exposures resulting in implantation of approximately 500 bacteria on each of days 1, 4, 8, 12 and 16. Exposure was calculated based on the CFU in the aerosol inoculum. The repeated exposure was calculated as the sum of the CFU/mL on each day of infection. (B) Frequency of cavitation among rabbits in the single exposure group and repeated exposure group. Cavities were identified by CT scan segmentation analysis as lung volumes not connected to the normal bronchial structure with densities between -875 and -1024 Hounsfield units, consistent with air. (C) The number of cavities per animal in the single exposure group and the repeated exposure group. Cavity counts are only plotted for the animals that demonstrated cavitation. (D) Quantification of the fraction of lung identified as diseased by gross observation for rabbits in the single exposure and repeated exposure groups.

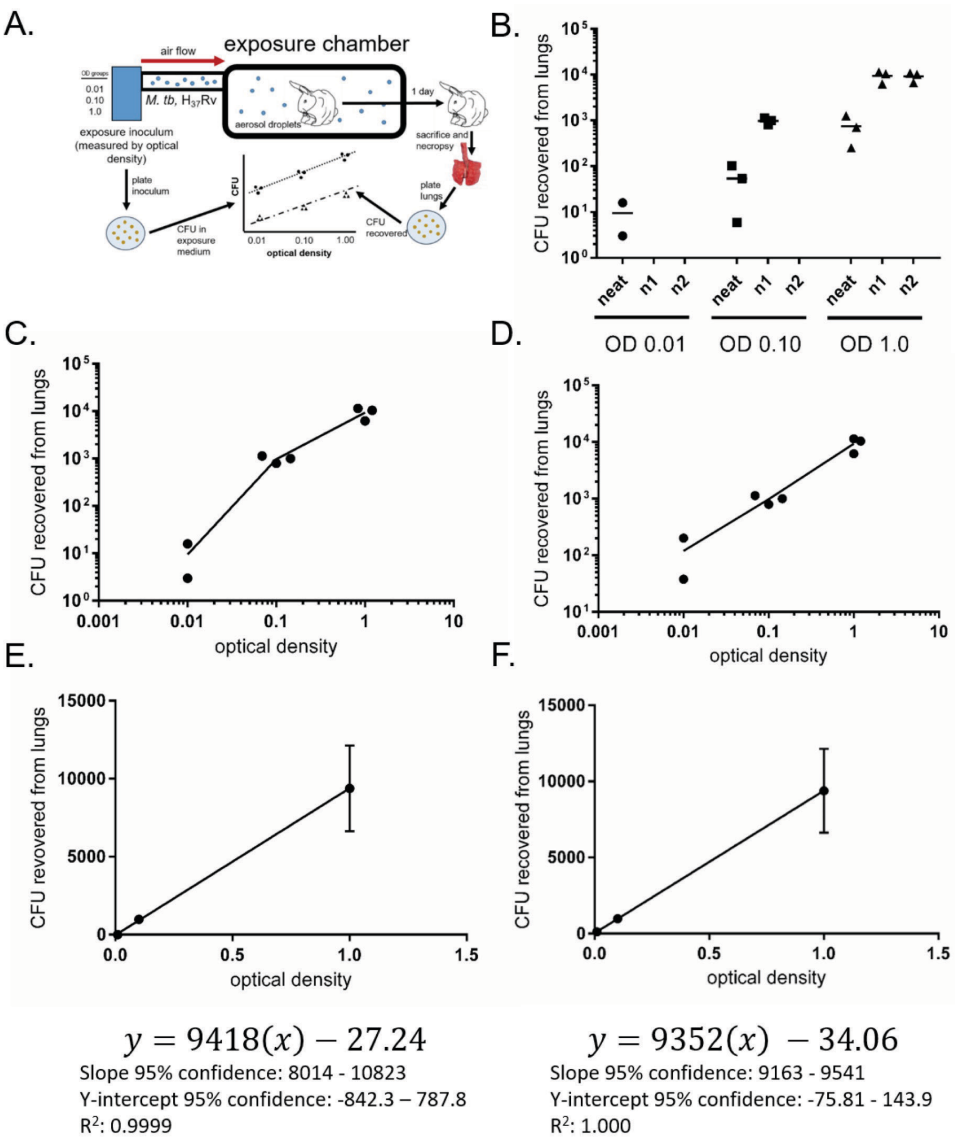

Figure 2.2: Titration of bacterial concentration in aerosol inoculum mapping optical density (OD) of aerosol inoculum to day-1 CFU recovered from rabbit lungs.
(A) Experimental outline. (B) Bacteria recovered from rabbit lungs reported by OD group and dilution. (C) OD mapped to CFU counts using 10x dilution in the OD 0.1 and 1.0 range, and neat (undiluted) counts in the OD 0.01 range. (D) OD mapped to CFU counts using 10x dilution in the OD 0.1 and 1.0 range. Counts in the 0.01 group were adjusted for tissue-homogenate CFU signal depression by multiplying OD 0.01 data-points by the ratio of average signal depression between 10x and neat dilutions in the OD 1.0 group (shown in B). (E) Best-fit linear regression for data in C. (F) Best-fit linear regression for data in D. All equations are calculated for the best-fit line between data-points.

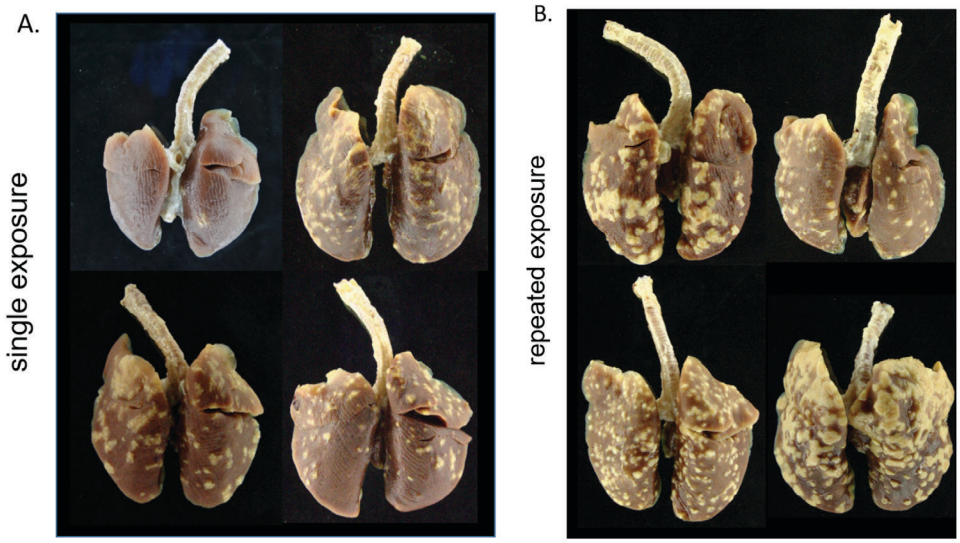

Figure 2.3: Gross images of formalin fixed lungs showing the dorsal aspect of the lungs.
(A) Lungs from rabbits in the single exposure group show a spectrum of mild to moderate disease. (B) Lungs from rabbits in the repeated exposure group show a spectrum of moderate to severe disease.

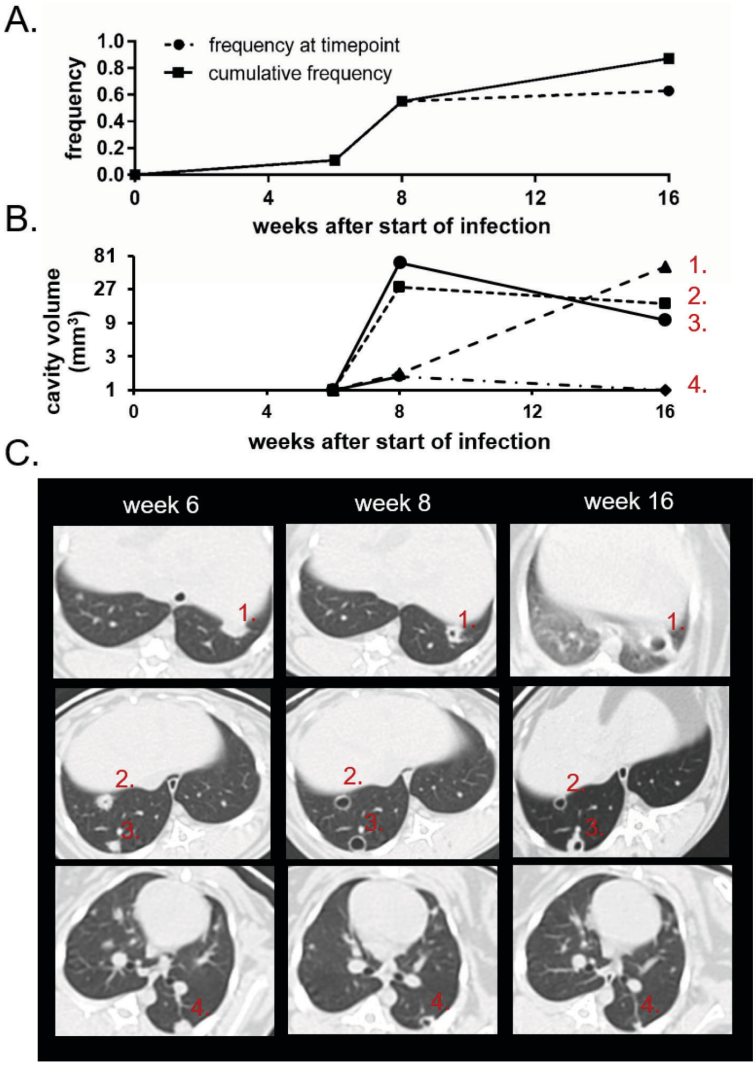

Figure 2.4: Timing of cavitation and cavity growth dynamics in the repeated aerosol method.
(A) The frequency of cavitation over time. The solid line indicates the cumulative frequency of cavitation among the cohort of 9 rabbits. The dashed line indicates the frequency of cavitation among the cohort at the specific time point and is distinguished from the solid line by the occurrence of cavity resolution. (B) Cavity volume mapped to time after the start of infection for four representative cavities demonstrating (1) continuous growth, (2, 3) growth and shrinking behavior, and (4) growth and resolution. Cavities were identified as lung volumes not connected to the normal bronchial structure with densities between -875 and -1024 Hounsfield units and points on the x-axis indicating a non-cavitary focus are plotted at the limit-of-resolution for the CT scanner. The y-axis is plotted using a logarithmic base 3 scale since measured volume varies closely as the cube of the radius of a spheroid object so that relationship among cavity volumes are more comparable to the two-dimensional reconstructions in C. (C) Transverse CT-scan reconstructions showing each of the foci identified in B. Transverse sections were chosen based on alignment of common anatomical markers outside the lung at each time-point.

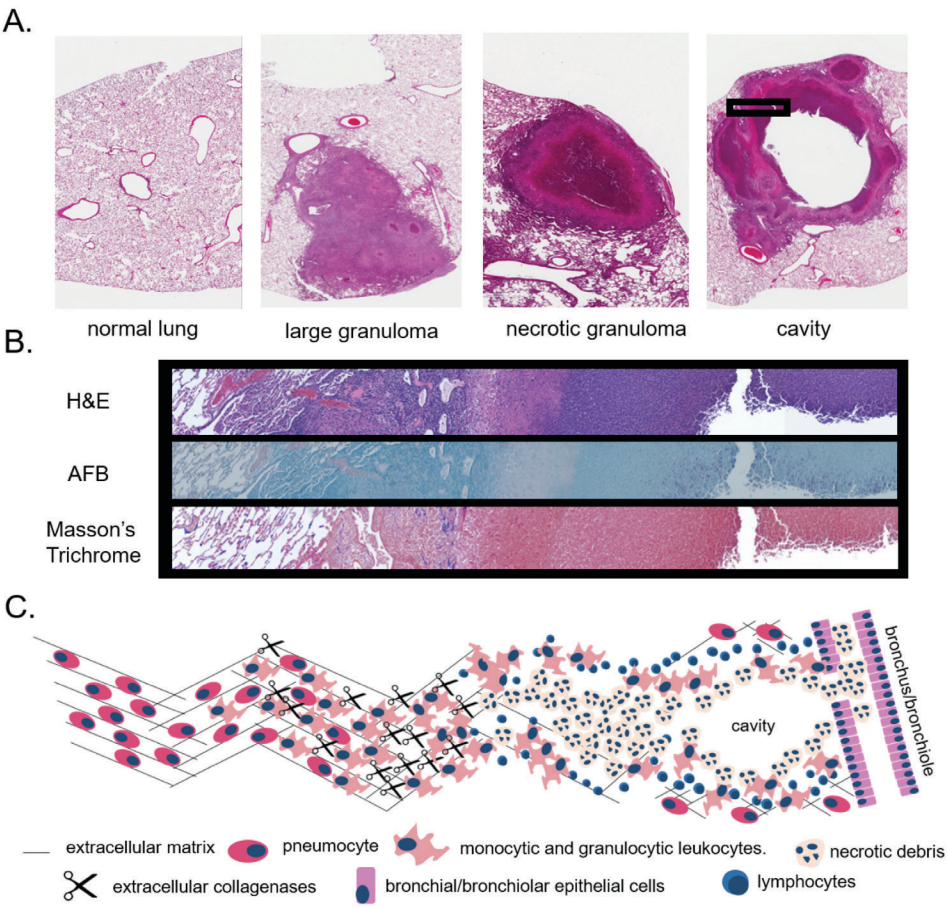

Figure 2.5: Histologic patterns of tuberculosis lesions in rabbits infected by repeated aerosol exposure. (A) Representative H&E stained formalin fixed tissue slides demonstrating lesions commonly observed in rabbits infected by repeated aerosol exposure. (B) Serial sections from the boxed region demarcated in A stained with hematoxylin and eosin, acid-fast, and Masson's trichrome stain. Masson's trichrome identifies collagen in blue hues. (C) Overview of the model for collagenase mediated destruction of extracellular matrix in proximity to a cavity.

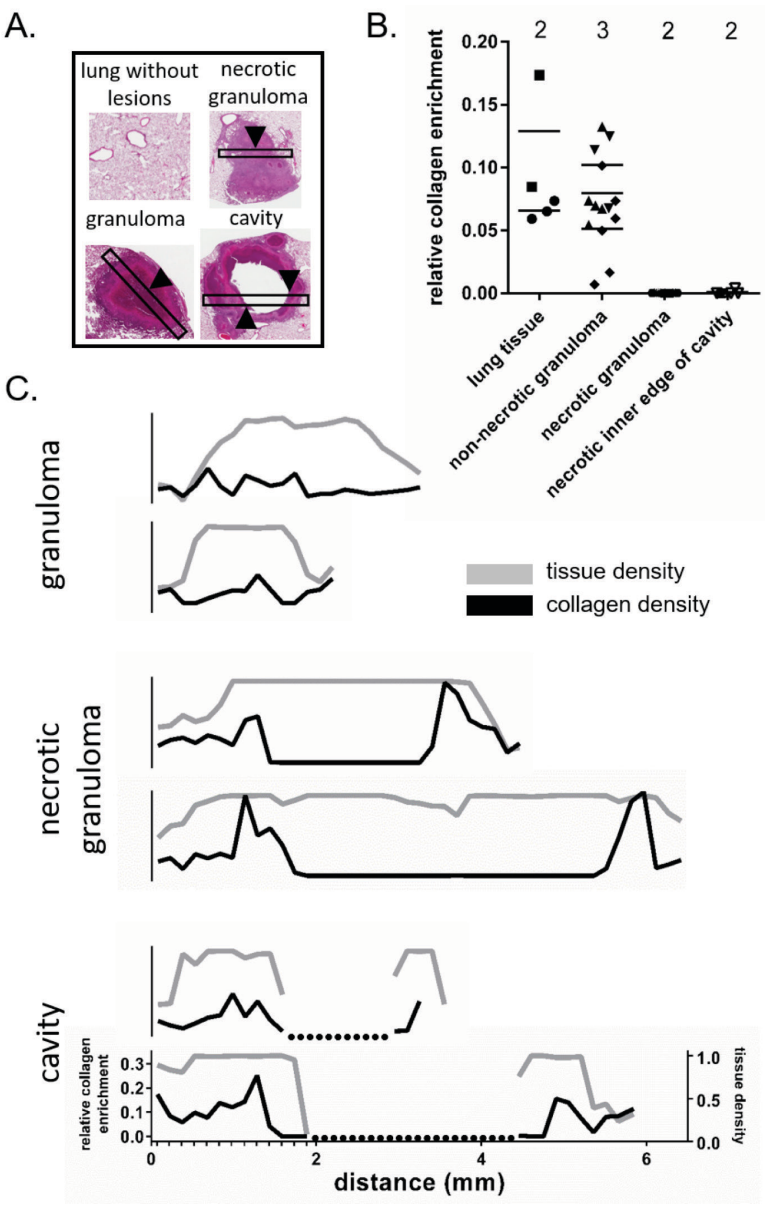

Figure 2.6: Collagen depletion in lung lesions of rabbits infected with *Mycobacterium tuberculosis*.
(A) Examples of fields used for quantification of collagen enrichment. Black rectangles represent example high-resolution fields used for quantification in B and traces in C. (B) Relative enrichment in collagen identified by blue hues in the Masson's trichrome stain. Surveys of collagen enrichment were random in normal appearing lung tissue and from regions 500 μm in length at the centers of lesion fields in granulomas and necrotic granulomas. Surveys of collagen enrichment from the cavity edge were defined as regions within 150 μm of the cavity edge. Multiple surveys were taken from non-overlapping areas within each region and the number above each category indicates the number of unique lesions surveyed. (C) Relative tissue density (grey line, right y-axis) and collagen density (black line, left y-axis) along linear traces crossing two granulomata, two necrotic granulomata, and two cavities. All traces are set to the same x and y scale as for the lower trace in E and the minor hash marks in E show the regular pattern of surveys continued along each lesion. Dotted lines indicate cavity space on histology.

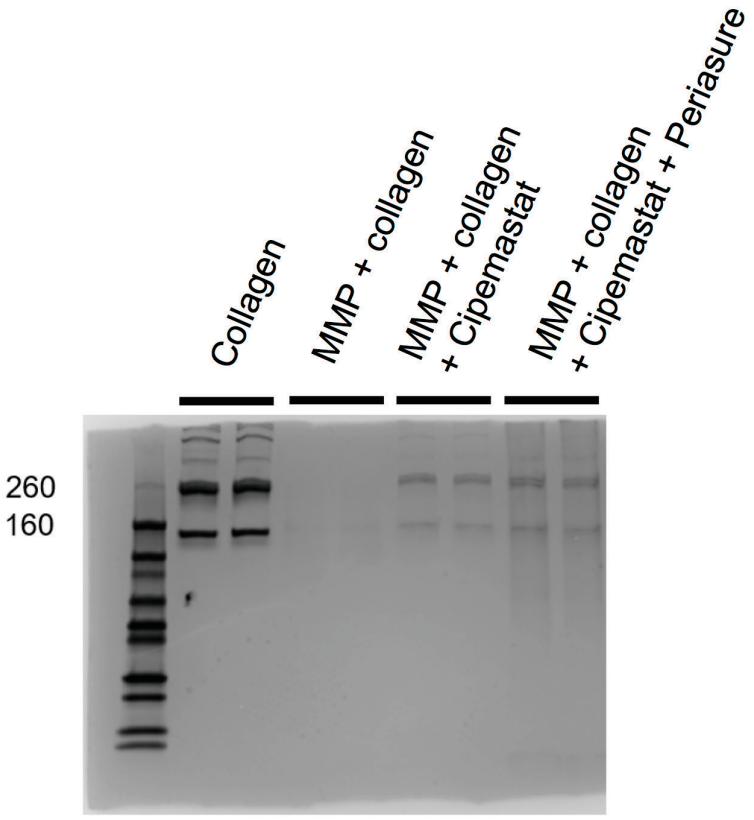

Figure 2.7: Coomassie blue stained gel electrophoresis of collagen incubated in the presence of human MMP-1, Trocade + MMP-1, and Troacade + MMP-1 in PediaSure vehicle.

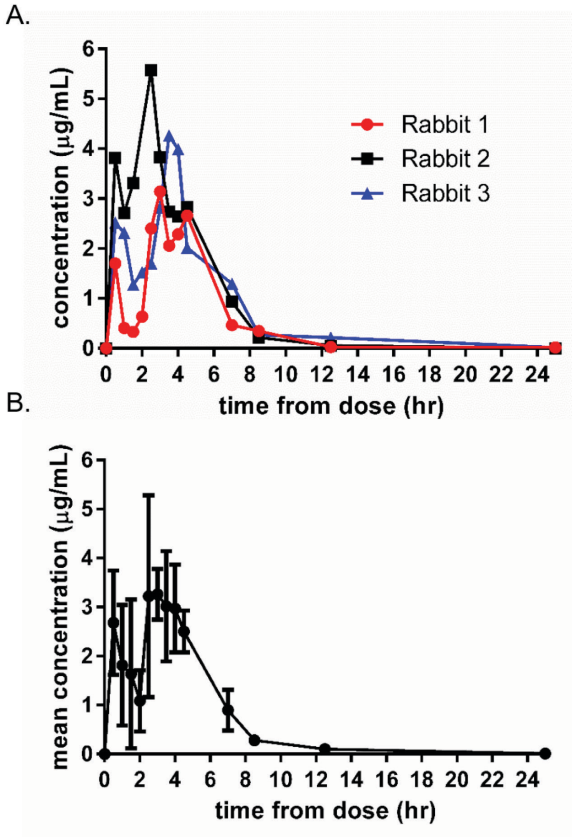

Figure 2.8: Plasma concentration curves relating the concentration of cipemastat in rabbit plasma following a single oral dose of 100 mg cipemastat/kg body weight.
(A) Graph showing traces for individual rabbits in the PK study. (B) Graph showing a curve representing the arithmetic means with standard-error bars of PK curves from the three rabbits shown in A.

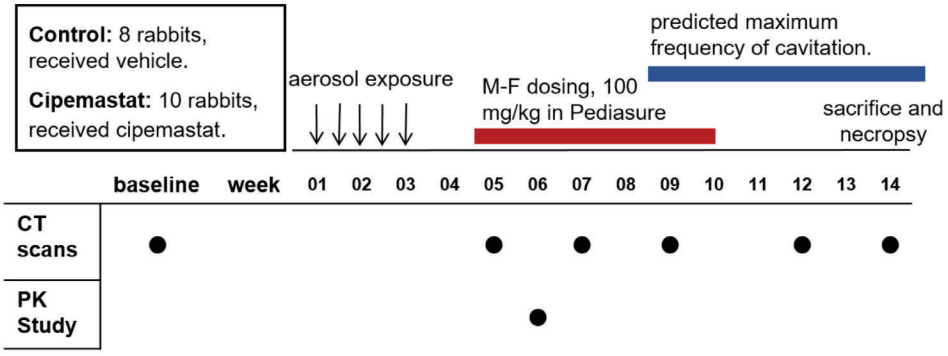

Figure 2.9: Experimental overview to investigate the pharmacologic inhibition of tissue destruction and cavitation using cipemastat in rabbits infected with *Mycobacterium tuberculosis*. The predicated temporal window for cavitation was designed based on data presented in Figure 2.2.

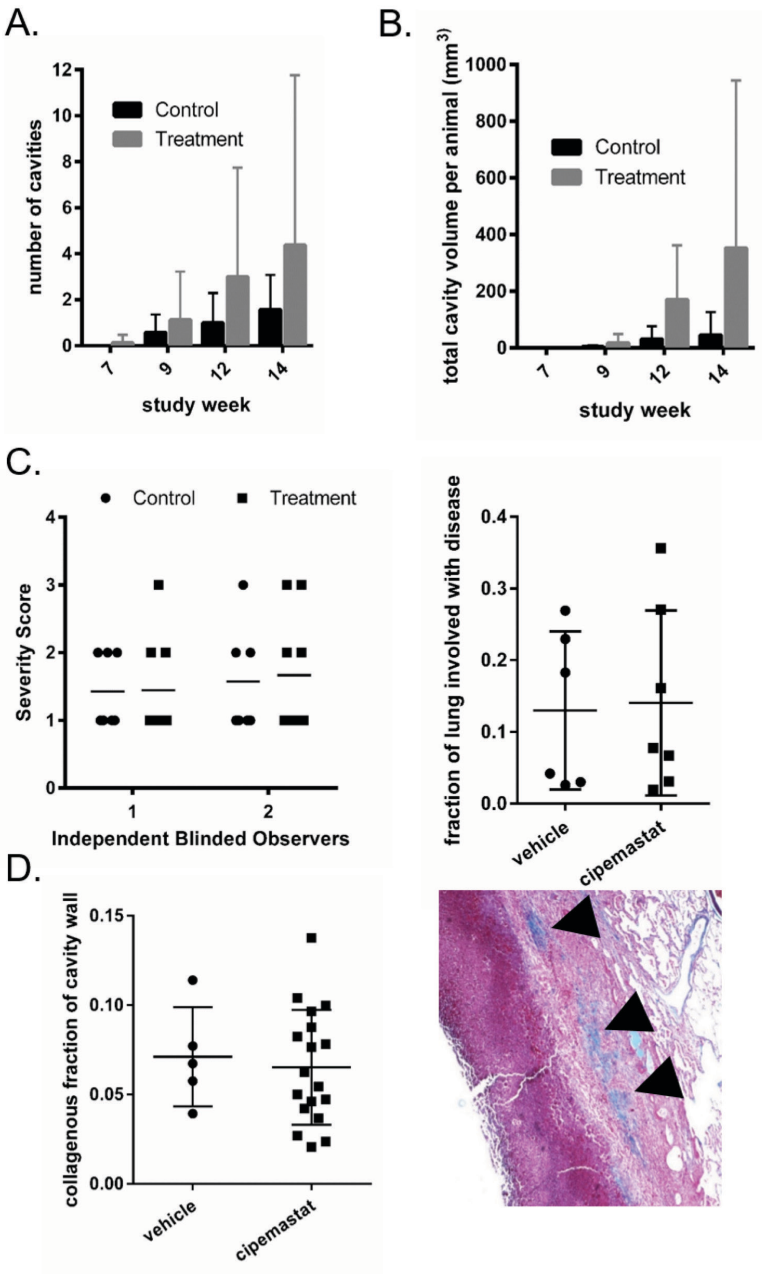

Figure 2.10: Collagen quantification in lung lesions of rabbits infected with *Mycobacterium tuberculosis*. (A) Average number of cavities per animal for weeks 7, 9, 12 and 14. (B) Average volume of the lung identified as cavity volume by CT-scan and segmentation analysis for weeks 7, 9, 12 and 14. (C) Disease severity scores of lungs assigned by two independent blinded observers. (D) Quantification of the fraction of lung identified as diseased by gross observation for rabbits in the single exposure and repeated exposure groups. (E) Example of a cavity wall showing regions identified as collagen. (F) Quantification of the collagen composition of cavity walls for cavities in animals treated with and without cipemastat.

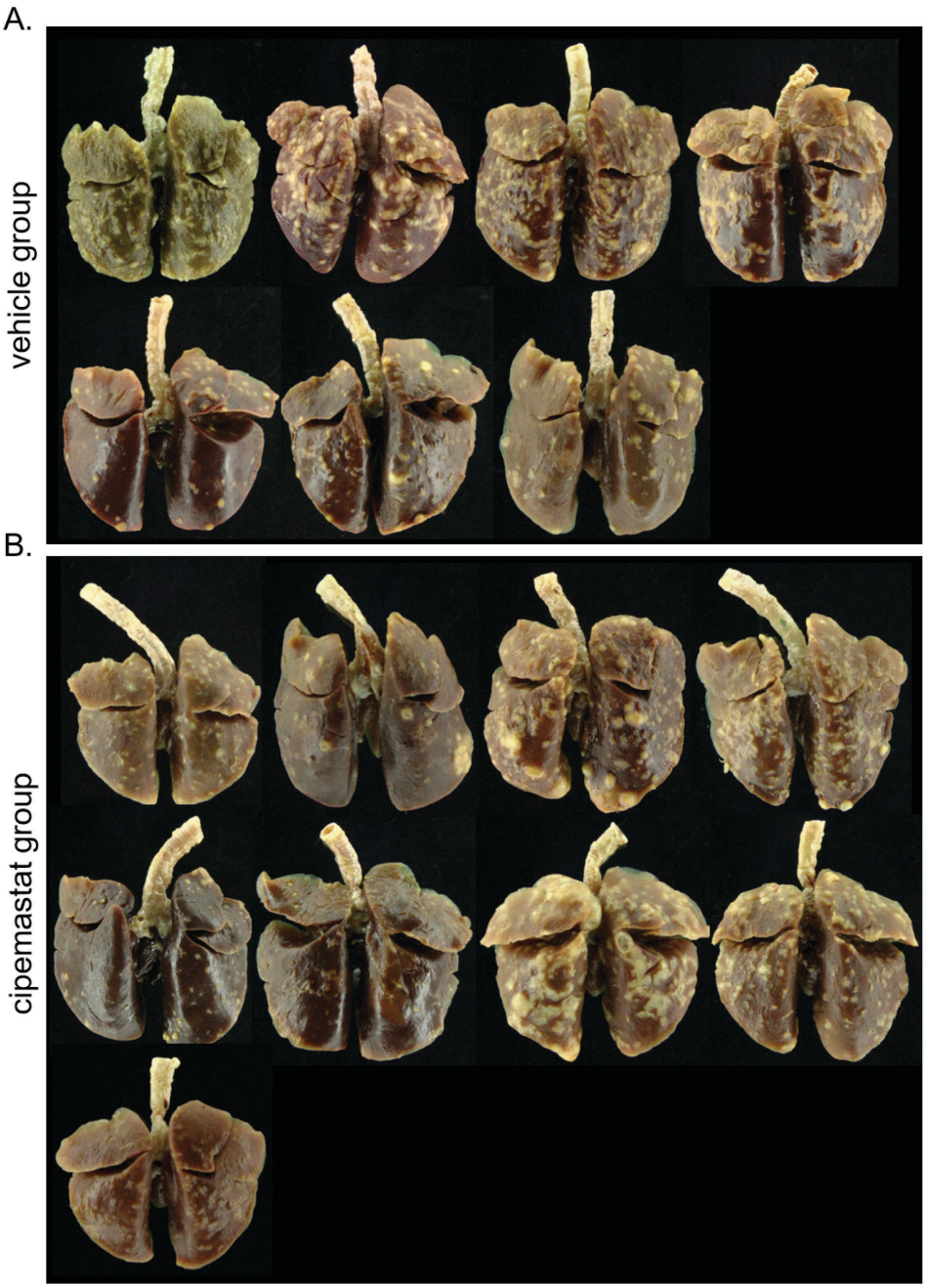

Figure 2.11: Gross images of formalin fixed lungs showing the dorsal aspect of the lungs.
(A) Lungs from rabbits in the vehicle treated group. (B) Lungs from rabbits in the cipemastat treated group.

Chapter 3

Mechanical Action on the Necrotic Granuloma Drives Tuberculous Cavitation

3.1 Background

Despite the availability and efficacy of current anti-mycobacterial drugs, tuberculosis (TB) continues to be a significant cause of morbidity and mortality worldwide [3]. To combat this persistent epidemic, research efforts have focused primarily on treatment and prevention with the development of new antibiotics and vaccines. However, the more difficult question of reducing transmission in high-burden countries has been insufficiently addressed. 30-50% of active TB infections result in the development of pulmonary cavities: abnormal air spaces surrounded by scar tissue which have replaced

the normal lung parenchyma [21]. Though not unique to TB, cavitation plays a central role in the epidemiology of tuberculosis by driving transmission, treatment failure and drug resistance [5,6,8,21]. The contribution of cavitation to the continued spread of TB makes it an attractive target for therapeutic intervention. However, despite the clear epidemiologic importance of cavitary disease, the pathophysiology of cavity development remains controversial.

A major challenge in interrogating cavitary disease is that, of the available animal systems used to model TB, few develop spontaneous cavitary disease that shows phenotypic similarity to the human counterpart [13,14]. Our lab has developed a reliable model of tuberculous cavitation using outbred New Zealand White rabbits infected with a serial low-dose exposure of *Mycobacterium tuberculosis*. This infection protocol was designed to mimic the pattern of human exposure in endemic environments. A high percentage of animals develop cavities by 7-9 weeks post-infection, and cavities display a high degree of phenotypic similarity to human cavitary lesions (Figure 3.1). Using high-resolution computed tomography in combination with gross and histopathology, we are able to follow cavities in real time and gain insight into the dynamics of cavity formation. By utilizing this infection protocol in conjunction with high-resolution CT scans, we demonstrate that mechanical factors play a significant role in cavity generation and maintenance.

3.2 Current Theories

The most widely accepted model of cavity formation proposes that cavities arise when large granulomas undergo central liquefaction, and subsequently erode into adjacent airways (Figure 1.1). Once in communication with the respiratory tree, these lesions discharge their liquefied contents, leaving behind an air-filled cavity. In this model, enzymatic proteolysis and matrix destruction are considered the major drivers of cavitation, and indeed, multiple matrix remodeling enzymes are known to be upregulated surrounding cavitary lesions [23,24,40–43]. With this body of literature, matrix metalloproteinases (MMPs) have emerged as promising potential therapeutic targets. While MMP inhibition in animal models demonstrably reduces extracellular matrix (ECM) turnover [44], cavity formation has not been reduced by agents that block MMP activity in mice or rabbits [25,45]. ECM depletion is expected to generate significant erosions into bronchioles and larger airways, and thus predicts sustained communication with the bronchial tree. Such cavities should have a well-aerated interior, with a similar gaseous composition to that of inspired air. However, studies by Haapanen *et. al.* revealed that a majority of human cavities have interior gas composition that is hypoxic and hypercarbic relative to alveoli, and frequently display either positive or negative internal pressure [46]. These findings agree with earlier work by Coryllos and others, who demonstrated cavities frequently contain pressurized interiors [47]. More recently, investigations by Belton *et. al.* revealed strong uptake of (18F)FMISO - an indicator of severe tissue hypoxia – in the consolidated region immediately surrounding pulmonary

cavities [48]. These findings demonstrate that sustained bronchiolar communication is not reliably present in a majority of cavities.

A second model of tuberculous cavitation proposes that cavities arise within the context of lipid pneumonia, independent of the granuloma. Drivers of cavitation in this model include bronchial obstruction by tuberculous pneumonia, and mycobacterial elaboration of cord factor [49,50]. Support for this model is based largely upon human autopsy studies from the 19th and early 20th century. Consequently, is difficult to link the identified lesions at autopsy with pre-mortem, serial 3D radiologic imaging (eg, CT scanning) and thereby establish a chronology of events leading to cavitation. Importantly, lipid pneumonia has not been linked with cavitation in animal models, the majority of which reveal that cavitation occurs within the context of the caseating granuloma [13,14,23,42].

Finally, the role of mechanical forces in the context of pulmonary cavitation appears as a persistently unanswered question over many decades of TB literature [51–56] and has recently received renewed attention [57,58]. The mechanical model of cavitation has its origins in the pre-antibiotic era, and postulates that cavitation is the result of the highly dynamic environment of the lung, which is subjected to constant motion and fluctuating pressures not experienced elsewhere in the body [33]. Pioneers of this model were the research surgeons of the pre-antibiotic era, who utilized iatrogenic pneumothorax in order to "rest" the lung and allow closure of the cavity. Though invasive, this was frequently successful [53]. This model is supported by the observation that cavities in man form preferentially in the apices of the lung, coinciding with the highest levels of pleural stress

[33]. Additional insight has been gained from comparisons to centrilobular emphysema and spontaneous pneumothorax, which have a similar preference for the lung apex [56,57]. Similar to the lipid pneumonia model, the mechanical model emphasizes the role of bronchial obstruction with formation of one-way valves that allow air to enter a cavity but prevent its escape [47]. Despite pulmonary mechanics being frequently cited as a probable contributor to cavitation, few investigators have attempted to clarify the role of mechanical stress in the pathogenesis of tuberculosis, likely due to limitations of current model systems.

3.3 Methods

Mycobacterial culture. Cultures of *Mycobacterium tuberculosis* H37Rv were growth from frozen stock aliquots in Middlebrook 7H9 liquid medium (Beckton Dickinson, Sparks, MD, USA) supplemented with 0.5% glycerol and 0.5% Tween 80.

Animal infection. 20 SPF adult female New Zealand White Rabbits, weighing 3.5 – 4.0 kg (Charles River Laboratories, USA and Robinson Services, NC, USA) were singly housed under Biosafety Level 3 conditions in accordance with protocols approved by the Institutional Animal Care and Use Committee at Johns Hopkins University, Baltimore, MD, USA. Infection was carried out using 5 low-dose aerosol exposures over a 2.5 week period using a Madison aerosol infection chamber (College of Engineering, University of Wisconsin, WI, USA). Delivery inoculum averaged 10^6 organisms per chamber cycle (6 animals per cycle), and animals were randomized between inoculations to minimize inter-cycle variability. This results in an implantation of approximately 500 CFU per animal

per exposure. CFU determination was calculated as previously described [13]. Sensitization was confirmed in all animals five days after the final inoculation by intradermal injection of 0.1 mL mammalian Old Tuberculin in the right flank (Zoetis, Parsippany, NJ). Induration was read at 48 hours, and was quantified by calculating the average skin fold thickness in two dimensions multiplied by the ratio of the thickness at affected to unaffected sites. All animals were visually inspected daily for signs of illness, including respiratory distress, or reduction in appetite, urinary or fecal output. Animals were weighed bi-weekly, at which time they received brief physical examinations by a licensed veterinarian.

Thoracic Computed Tomography (CT). Animals were sedated with intramuscular injections of xylazine (3 mg/kg), ketamine (25 mg/kg) and acepromazine (1 mg) prior to bronchoscopically–assisted intubation with a 3.5 mm endotracheal tube (Teleflex Medical, Research Triangle Park, NC). Following intubation, anesthetized animals were placed into a sealed chamber for transport to an imaging suite, where they were maintained on injectable anesthesia and 1-3 L/min oxygen. Breath-hold image acquisition was performed as previously described [22]. Sedation was partially reversed with IV yohimbine (0.1 mg/kg) as needed. All animals were imaged at baseline (prior to infection), and then at 5, 7, 9, 11-12 and 14 weeks post-infection on a CereTom portable CT scanner (NeuroLogica, Boston MA).

Image Processing. Raw CT scan data was compiled into DICOM files using Loening Amide (Version 0.9.0). All image analysis was performed using Invicro VivoQuant software (Version 2.50). Cavities were defined as having a central radiodensity matching

that of aerated lung (-1024 to -725 Hounsfield Units [HU]), surrounded by a radiodensity matching that of soft tissue (> -725 HU), which had a spherical morphology in three dimensions. Cavities that were not identified on at least two consecutive time points (including necropsy) were excluded from analysis to minimize the inclusion of radiographic artifacts. Gross photographs were analyzed in ImageJ (version 1.49, NIH, USA) by manually segmenting diseased lung and calculating extent of disease as the ratio of involved to uninvolved lung in ~5mm transverse lung sections.

Necropsy and histopathology. IM sedation was performed as previously described, after which animals were euthanized with 2-3cc IV pentobarbital solution in the marginal ear vein. Immediately following euthanasia, the lungs were isolated and gently infused with 10% neutral buffered formalin prior to fixation. Tissues were fixed in 10% neutral buffered formalin for 48 hours, at which time they were serially sectioned, photographed and processed for histology. 5 μm paraffin-embedded sections were stained with hematoxylin & eosin (H&E), or Masson's trichrome. Image capture for semi-automated quantification of trichrome staining was performed on a Nikon Eclipse 90i microscope with attached Nikon DS-Ri1 color camera, and analyzed using NIS Elements Advanced Research software (Version 4.50, Nikon Instruments, Melville, NY). Region of interest (ROI) selection was performed manually, and included the entire thickness of the cavity wall while excluding the interior air space. Positive staining was then calculated as a percentage of the total ROI.

Statistical Analysis. All statistical analysis was performed with GraphPad Prism (Version 7.0, GraphPad Software, San Diego, CA). Single-variable data were analyzed

by nonparametric Kolmogrov-Smirnov test to compare cumulative distributions. Paired data were analyzed by nonparametric Wilcoxon test. Data sets containing three or more groups were analyzed by one-way ANOVA with Kruskal-Wallis test. Degree of correlation was calculated by liner regression with Spearman correlation coefficients and 95% confidence interval. All error bars represent mean and standard deviation.

3.4 Results

Cavities show rapid expansion compared to solid caseous lesions. Cavitation was observed beginning at week 7 post-infection (PI), with the majority of cavities arising between 9-14 weeks PI. High inter-animal variability was observed in terms of disease severity and cavity generation, with 65% (13/20) of animals developing at least one cavity, and 69% (9/13) of those developing more than one cavity. Cavity size varied considerably, both within and between animals (Table 3.1).

Cavitation was invariably preceded by a region of dense consolidation, identified as pulmonary regions with radiographic density matching that of non-aerated soft tissue (> -725 Hounsfield Units [HU]) (Figure 3.2A, 3.2B). To examine how cavities transition from these areas of solid consolidation, we compared total lesion volume ($V_{consolidation}$ + V_{cavity}) between sequential CT time points, with V2 representing the first appearance of the cavitary lesion, and V1 representing the region of consolidation at the time point immediately preceding cavitation. The V2:V1 ratio was then used to assess the rate of growth for each lesion. We discovered that cavity growth is rapid and abrupt, with cavity volumes ranging from 0.67 to 9.30 times the volume of the regions of consolidation from

Animal ID	Cavity ID	Week 7 volume	Week 9 volume	Week 12 volume	Week 14 volume
2	2.1	0	8.24	1.7	0.24
	2.2	0	0	107.79	0.12
3	3.1	0	0.61	17.08	7.02
	3.2	0	0	10.29	4.24
	3.3	0	10.05	3.15	0
4	4.1	0	0	0	188.92
6	6.1	0	0	15.62	14.65
	6.2	0	0	0	1.09
	6.3	0	4.97	0.48	7.51
	6.4	0	0	0	2.18
10	10.1	0	208.42	75.93	4.84
	10.2	0	133.09	19.13	9.57
11	11.01	0	0	0	1.93
	11.02	0	33.06	35.6	29.79
	11.03	0	0	0	1.7
	11.04	0	0	0	5.57
	11.05	0	0	0	1.21
	11.06	0	0	13.32	1.57
	11.07	0	7.75	5.69	17.8
	11.08	0	0.73	12.95	19.5
	11.09	0	0	10.78	1.45
	11.1	0	0	3.39	7.02
	11.11	0	0	50.86	7.63
	11.12	0	0	48.84	9.33
	11.13	0	0	34.27	8.48
	11.14	0	0.84	78.11	5.45
	11.15	0	0	0	33.06
	11.16	0	0	0	25.92
	11.18	0	1.7	17.08	0
	11.19	0	20.47	9.33	3.03
13	13.1	0	0	0	0.48
	13.2	0.48	2.06	12.84	0
17	17.01	0	0.24	274.3	1083.64
	17.02	0	0	22.89	63.34
	17.03	0	0	2.79	5.81
	17.04	0	0	13.32	0.73
	17.05	0	5.81	4.24	19.01
	17.06	0	0	0	2.42
	17.07	0	1.57	1.33	1.33
	17.08	0	0	1.57	5.57
	17.09	0	0	1.21	6.78
	17.1	0	0	0	41.41
	17.11	0	0	0	0.85

Table 3.1: Changes in cavity volume over time.

which they arise. On average, cavities were 1.87 times larger than their respective consolidated foci. We then compared this with the growth rates of solid, non-cavitary

lesions over the same time frame (sequential time points between weeks 7-14) using the above method. The behavior of solid lesions was significantly less dynamic, with growth rates ranging from 0.47 to 1.57. Surprisingly, 78% of non-cavitary lesions examined had a V2:V1 ratio less than 1, indicating that the majority of solid lesions shrunk over this time period. (Figure 3.2C).

After formation, cavity behavior was highly variable, with cavities falling into one of three groups. The majority of cavities (17/32) were largest at the time of initial detection, and then progressively contracted over subsequent time points. A second group of cavities (8/32) underwent gradual enlargement from the time of detection. This group included several of the largest cavities. Finally, a third group (7/32) was characterized by small size (< 100 mm^3) and dynamic behavior with alternating growth and shrinkage (Figure 3.2D). 4% of cavities (3/79) underwent complete resolution, becoming undetectable on both radiography and gross pathology. Remarkably, resolution did not correspond to any specific growth pattern. Of the three cavities that resolved completely, one fell into each of the above groups (growing, shrinking and dynamic).

Disease is evenly distributed throughout the lung, but cavitation occurs at regions of high mechanical stress. As cavitary disease in human patients disproportionally affects the apices of the lungs, we sought to identify if cavities in rabbits also displayed a bias toward specific lung regions. Although there was no significant difference in the distribution of solid lesions in the lungs (Figure 3.3A), pulmonary cavities were unevenly distributed throughout the lung, with significantly more cavities forming in the caudal lobes (Figure 3.4A). In order to determine the effects

of transpulmonary pressures on cavity formation, a plane was drawn on CT images parallel to the course of the primary bronchi at the level of the tracheal bifurcation. This separated the lung into cranioventral (CV) and caudodorsal (CD) lung fields, corresponding to the sites of lowest and highest transpulmonary pressure in quadrupeds respectively [59]. We found that significantly more cavities formed in the caudodorsal lung fields when compared to the cranioventral regions, on both a total and per-animal basis, with animals having roughly twice as many caudodorsal cavities on average (Figure 3.4B). Cavities in the caudodorsal fields were also larger than those in the cranioventral regions, and associated with significantly more collagen deposition (Figure 3.4C, 3.4D). Irrespective of lung lobe, cavities usually (33/49) displayed a subpleural localization, where they were associated with varying degrees of pleural inflammation and fibrosis (Figure 3.4E). Surprisingly, despite frequent proximity to the pleural space, there was no evidence of cavitary rupture or pneumothorax, although occasional fibrinous adhesions between the visceral and parietal pleura were noted in several animals on postmortem examination.

Cavitation occurs exclusively in the context of necrotizing granulomas with variable airway communication. Histologically, 100% (49/49) of examined cavities occurred within the context of organized granulomas, composed of discrete layers of epithelioid macrophages, multinucleated giant cells and lymphocytes, surrounded by fibroblasts and partially encapsulated in mature collagen. Cavitating granulomas were universally associated with central necrosis, as evidenced by a variably thick rim of acellular granular debris lining the cavity interior. Organized granulomatous

inflammation with central necrosis was a feature of all cavities examined, regardless of lesion age, size, morphology or location within the lung. While cavitation was invariably associated with necrosis, the converse was not true. Large necrotic granulomas without evidence of central cavitation were frequently visualized, suggesting that necrosis is necessary but not sufficient for the development of cavities (Figure 3.1C). Airway communication, defined as histologic continuity of the cavity interior with ciliated columnar respiratory epithelium, was detected in only 16% (8/49) of examined cavities (Figure 3.4E). These microscopic connections were below the limit of radiographic detection, and were not identified on computed tomography. As such, this figure likely underestimates the prevalence of bronchiolar communications. Based on gas and pressure analyses performed by Haapanen, roughly 33% of cavities are predicted to have sustained open communication with an airway [46].

Our observations that rabbit tuberculous cavities (i) expand abruptly, (ii) appear subpleurally in the caudodorsal lung fields which experience the highest transpulmonary pressure, and (iii) form exclusively from pre-existing necrotic granulomas are consistent with cavity biogenesis resulting from acute tears in areas of necrotic tissue, with rupture into small airways and rapid subsequent gaseous filling.

Cavities show divergent histomorphology with four discrete lesion types that provide mechanistic clues. Histologic examination of cavities revealed four distinct lesion morphologies (Figure 3.5A). The dominant morphology - designated as “smooth” – was characterized by a sharply-defined gas tissue interface at the cavity interior (Figure 3.5B). This morphology was seen in over half of the cavities examined (27/49). The least

common morphology ("rough," 4/49) had an interior cavity surface with an ill-defined, ragged gas-tissue interface (Figure 3.5C). A third type ("mixed," 13/49) displayed characteristics of both rough and smooth cavities, with only a portion of the interior having the crisp and well-demarcated gas-tissue interface that defined smooth cavities (Figure 3.5D). The commonality of these three types was the relative thickness of the cavity wall. Smooth, rough and mixed cavities contained variable amounts of necrotic debris at the interior surface, and were surrounded by a thick wall of organized granulomatous inflammation. Finally, a small subset of cavities (5/49) – designated as "fibrous" - were characterized by large size and extremely thin walls composed almost entirely of mature fibrous tissue, and a slender, discontinuous inner rim of necrotic and inflammatory debris (Figure 3.5E).

Next, we examined the relationship between lesion morphology and lesion age, defined as the time from first CT appearance of the cavity to the time of cavity resolution or necropsy. Unexpectedly, cavities with smooth or fibrous morphology represented the youngest lesions (Figure 3.5F). A potential confounder in this analysis is the fact that 4% (3/79) of cavities had resolved by the time of necropsy, making it impossible to define their cavity types. Thus it is possible that spontaneously resolving cavities belonged to a particular cavity type which would be underrepresented in the analysis above.

All cavities were stained with Masson's trichrome to assess the amount of collagen in each lesion as a percentage of the total cavity wall, which excluded air and necrotic debris at the cavity interior. Not surprisingly, fibrous cavities displayed the highest amount of collagen as a total percentage of their wall, but there was no significant

difference in collagen content among the other three cavity types (Figure 3.3B). Remarkably, the amount of fibrosis did not correlate with the age of the lesions (Figure 3.3C).

Tuberculin reactivity and disease severity do not predict the extent of cavitation. Previous work by Converse [17] and Kubler [22] demonstrated a weak correlation between the degree of tuberculin reactivity and the extent of cavitation using a small number of animals. In the present study, no significant correlation was found between induration and either the severity of disease or the number of cavities generated (Figure 3.6A, 3.6B). Somewhat unexpectedly, the extent of grossly-visible disease was also not predictive of cavitation, and animals with minimal disease occasionally generated large numbers of cavities (Figure 3.6C).

3.5 Discussion

Using a longitudinal imaging approach in combination with histopathology, we demonstrate that cavities expand rapidly upon development and then may resolve, continue to grow, or wax and wane in size. Far from being a new observation, the dynamic nature of cavities appears as a common source of frustration as far back as the early 1900's, with Coryllos anthropomorphically relating their behavior as "capricious and puzzling [53]." When comparing the growth kinetics of cavities to solid lesions, it is apparent that there are mechanisms at work other than simple evacuation of interior contents. One would expect cavities growing by simple liquefaction and evacuation to be similar in size to the solid lesions that precede them. However, most cavities in this study

were several times larger than their corresponding precursor lesions, suggesting an explosive growth event. Additionally, the observation that most cavities are largest at the time of initial presentation strongly suggests that the onset of cavitation is an acute event, rather than a slow emptying of contents. The surprising observation that the amount of lesion fibrosis does not correlate with the age of the lesion confirms that remodeling of the fibrotic wall is similarly dynamic.

In humans, cavitary lesions show a strong preference for the apices of the lung [12]. Based on this distribution, it has long been presumed that cavities form preferentially at sites of high ventilation:perfusion (V:Q) ratios which favor bacterial growth [58]. However, in addition to receiving the highest relative ventilation, the apices of the human lung are also the site of highest mechanical stress. Transpulmonary pressure (TPP), the "tension" force applied to the lung by negative pressure within the pleural space, follows a vertical gradient due to the interactions of gravity and thoracic wall shape. In humans, the area of greatest TPP therefore corresponds to the apices of the lung [33,56], while in quadrupeds, the caudodorsal lung fields experience the highest TPP [59]. Meanwhile, V:Q ratios in animals are more uniformly distributed throughout the lung, owing to the effects of body posture on blood flow [60,61]. This critical species difference has allowed us for the first time to tease apart the relative contributions of V:Q and TPP to the cavitation process.

Our observation that rabbit tuberculous cavities are 2-fold more likely to form in the caudodorsal lung fields in the face of uniform disease indicates that TPP gradients play a significant role in determining cavity distribution. Additionally, these cavities are also larger, and display significantly increased collagen deposition when compared to those at

low TPP sites. This is likely due to the well-known effects of biomechanical instability on collagen deposition in damaged tissue [62,63]. These results expand on the findings of Medlar and Sasano, who reported that maintaining infected rabbits in an upright posture alters the distribution of their disease to a more "human" phenotype with localization at the apices [64]. Recent investigations by Casha *et al.* further emphasize the role of mechanical stress in human cavity development. Using computer modeling techniques, they demonstrate the profound effect that thoracic wall shape has on pleural stress, especially at the apex of the lung. In low BMI chests, they discovered up to a 10-fold increase in pleural stress at the apex, potentially explaining the increased incidence of cavitary TB in young males and individuals with low BMI [57].

A majority of cavities in this study occurred subjacent to the pleura, further supporting the hypothesis that cavities occur at regions of structural weakness. Lesions occurring here are not surrounded by a buffer zone of elastic alveoli, but instead face the pleura which contains a higher proportion of inelastic collagen. In the face of high regional TPP, this area is predisposed to tears, evidenced by the high frequency of subpleural "blebs" and bullae in other pulmonary diseases such as emphysema [56,57]. Studies of patients with pleural tuberculosis (arising from extension of subpleural lesions) report the incidence of subpleural cavitation at 50-60%, but the fraction of cavities which form subpleurally is unclear [65]. Cavitation is not unique to TB, and may be caused by a diverse group of infectious etiologies as well as several neoplasms. The fraction of subpleural cavities has been documented for several other diseases, and in some infections approaches 100% [21].

Histologic examination of a large number of lesions revealed the existence of distinct cavity types. Over half of cavities displayed a sharply-demarcated gas-tissue interface, identical to those observed in the emergent C3HeB/FeJ mouse model of cavitation [42]. Similar morphology has been referenced in detailed pathologic descriptions by Sweany and Seiler, who describe cavities with "smooth walls," and provide photomicrographs of human cavities with clear "mixed" and "fibrous" morphology [66] (Figure 3.1D, 3.1E), confirming the translatability of findings in the rabbit model. This smooth histologic appearance is not pathognomonic but is distinctive of lesions where gas exerts pressure on surrounding tissue. Other diseases that share this morphology include Clostridial gas gangrene [67], decompression sickness [68], and gas bubble disease in aquatic species [69], in which the production or traumatic inoculation of gas bubbles produces the appearance of compressed tissue surrounding a central air space. The gross appearance of large gas bubbles dissecting through tissue planes [68] brings to mind Coryllos's descriptions of a mucosa-like "glistening lining membrane" within many cavities, and also undeniably resembles the smooth shiny cavitary interior seen frequently in this model (Figure 3.1A).

In the context of tuberculosis, these smooth-type cavities suggest a novel mechanism for cavity formation (Figure 3.7). The necrotic granuloma is fundamentally a sphere with a rigid fibrotic exterior and a soft caseous interior. Inspiration produces a rapid drop in pleural pressure, translating to the application of external tension and development of negative pressure within the sphere. Fibrous tissue is inelastic, and therefore prone to failure under repetitive mechanical stress. A tear occurring in the fibrotic wall that extended to the necrotic center would allow air to be sucked into the soft interior on

inspiration, with rapid subsequent enlargement of the lesion. Upon expiration, the tension force would be released resulting in positive pressure within the lesion and temporary closure of the tear. This is similar to the "one-way valve" theory postulated by Coryllos, Eloesser, and others, and explains the finding that cavities frequently contain pressurized interiors [47,53,54]. Cavities with "smooth" morphology are younger on average, confirming that this most likely represents an early stage of cavitation. An extreme example of air-trapping may also explain the presence of similarly young "fibrous" type cavities, with their large central space and thin walls reminiscent of balloons. Experiments by Coryllos in 1938 corroborate this mechanism by the introduction of a small diameter thoracoscope into human cavities and injection of small amounts of dye or saline. When suction was applied to the cavity interior, Coryllos observed a "bubbling of air" inward through the bronchial outlet, with simultaneous drainage of the instilled fluid. However, when positive pressure was applied, no movement of air or saline occurred, indicating that the outlet had been temporarily obstructed [47].

Our findings strongly support a mechanism of cavitation driven by mechanical action on the necrotic granuloma. However, the question of the role of matrix remodeling enzymes in cavitary pathogenesis remains. In addition to driving a number of pathologic conditions, MMPs play an essential physiologic role in wound repair [70]. Tissue injury by any means produces a secondary increase in matrix remodeling enzymes, and these elevations persist in the case of chronic non-healing wounds. Thus, elevated levels of MMPs and other ECM modifying enzymes may reflect their action as secondary responders to tissue injury, rather than primary drivers of cavitation. Regardless of the

initiating cause, it is likely that proteolysis and mechanical forces ultimately act in concert to produce tears in structurally weakened tissue.

Investigative pathology necessitates a "snapshot" approach that often makes determining a sequence of events challenging, if not impossible. For this reason, precursor lesions were documented radiographically for each cavity, and used to determine growth kinetics. There has been extensive discussion of "liquefaction of the caseum" as the critical event preceding cavitation by Canetti, Dannenberg and many others [12,58,71], which has induced a decades-long search for the missing link in cavity pathogenesis. The lack of grossly liquefied caseum in this model (in contrast to high-dose bronchoscopic and M. bovis infection models) combined with the higher incidence of observed cavitation [25] argues against the existence of a transitional lesion requiring liquefied caseum. Our data suggest that a cavity is merely a traumatized necrotic granuloma, and predict that the lesion that gives rise to a cavity is histologically indistinguishable from any other caseating granuloma. This is supported by the observation that residual caseum within a cavity is microscopically identical to caseum inside a solid necrotic granuloma in both humans and rabbits [14] (Figure 3.1).

In summary, this study employs a rabbit model of cavitation which produces a high frequency of human-like cavities, serial high-resolution CT scanning, and careful histopathologic analysis to chronicle the kinetics, distribution, and histologic types of tuberculous cavities. Our data support a mechanism of cavitation in which mechanical intrapulmonary forces act on the necrotic granuloma to produce a cavity. Although more studies are needed to confirm the findings here and their translatability to human patients,

elucidation of these mechanical factors may give additional insight on the lung-specific nature of cavitation. We also show further support that necrosis is an absolute prerequisite for cavitation. As intrapulmonary mechanical action cannot be easily altered, future studies should endeavor to prevent necrosis as a means of inhibiting cavitation.

Figures

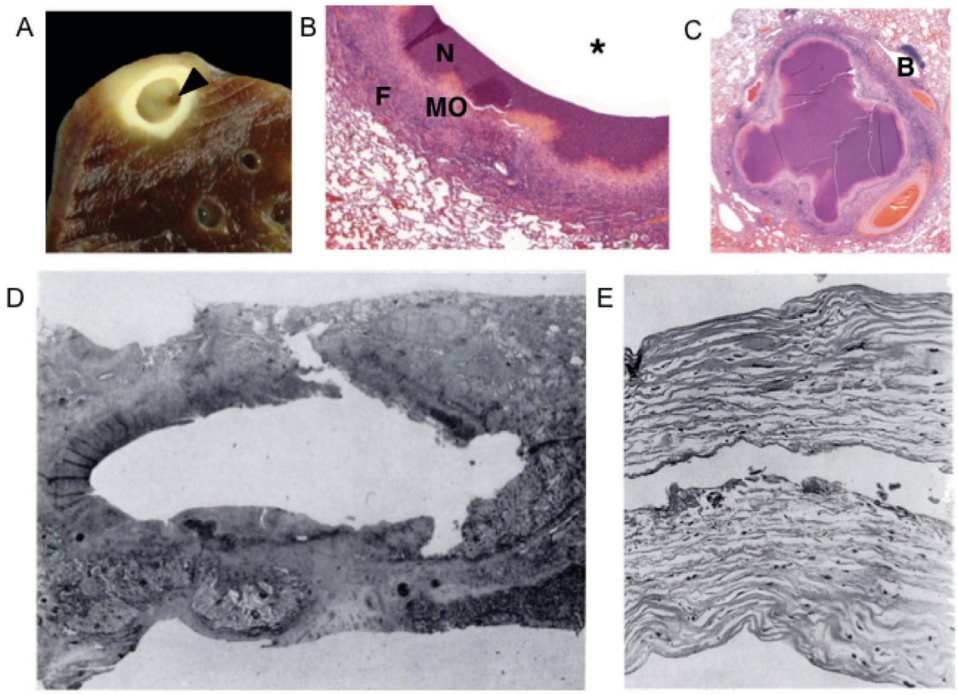

Figure 3.1: The rabbit model of tuberculous cavitation reliably produces lesions with a high degree of similarity to human cavities.
(A) Transverse lung section showing gross pathology of a single subpleural cavity. The interior surface of the cavity is smooth and glistening. A small outlet is visible leading out of the cavity (arrowhead). (B) Histopathology of rabbit cavities shows homologous morphology to human cavities, with a central air space "*" surrounded by necrotic debris "N", layers of epithelioid macrophages "MO", and fibrous connective tissue with scattered lymphocytes "F". H&E. (C) Low-power view of a large necrotic granuloma without evidence of cavitation, despite close proximity to a bronchus “B”. Note the appearance of the central caseum, which is indistinguishable from casum lining a newly-formed cavity. H&E. (D) Photomicrograph of a pulmonary cavity from a human patient, showing “mixed” morphology. On the left, the interior surface of the cavity forms a sharply-demarcated gas-tissue interface. To the top and right, residual caseum at the cavity wall has begun to crumble. H&E. (E) Two walls of a “tension-type” or “bullous” cavity from a human TB patient, described as “thin plates of connective tissue.” A small amount of necrotic debris lines part of the cavity interior. Inflammatory cells are absent. H&E. D+E Reproduced with permission from the American College of Chest Physicians (1956).

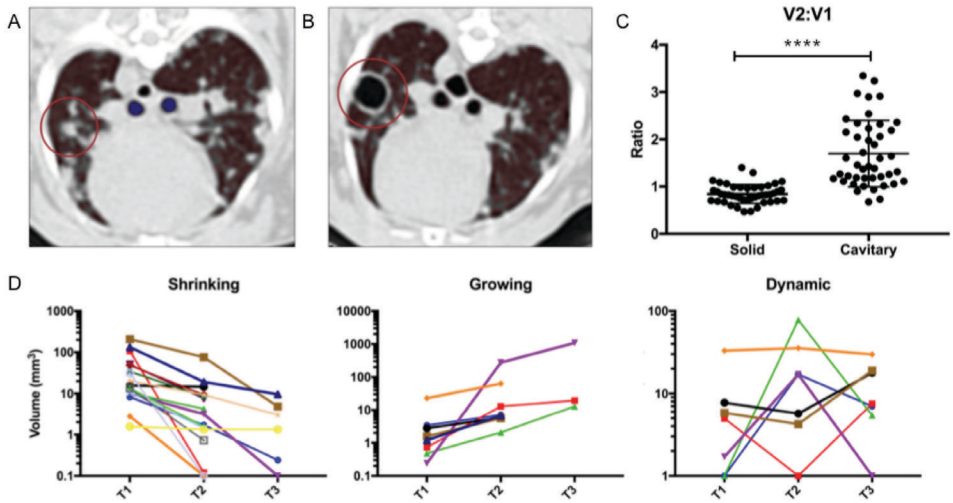

Figure 3.2: Cavities arise rapidly from areas of pulmonary consolidation, and show highly dynamic growth kinetics.
(A) Mid-thoracic transverse CT of an infected rabbit at week 7 post infection (PI) demonstrates a focus of pulmonary consolidation 4.4 mm in diameter, with no evidence of cavitation (circled). (B) Mid-thoracic transverse CT of the same animal at week 9, showing a large air-filled cavity present in the area of previous consolidation, measuring 8.8 mm in diameter (circled). (C) Growth rates of solid and cavitary lesions during week 7-14 PI, where V1 and V2 represent the lesion volume at two sequential timepoints. $p < 0.0001$ (****), Kolmogorov-Smirnov paired t test. Mean & standard deviation (SD). (D) Growth dynamics of cavitary lesions during week 7-14 PI, where T1 represents the first appearance of the cavity, T2 and T3 represent sequential timepoints following the cavitation event. Each colored line represents a single cavity.

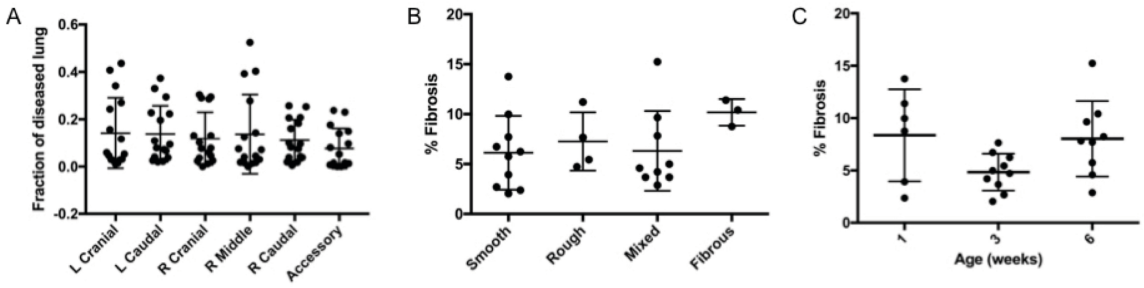

Figure 3.3: The amount of intralesional fibrosis does not correlate to lesion age or morphology.
(A) Lesions are evenly distributed throughout all lung lobes. Each point represents a single animal. Disease fraction was determined by using 5mm thick cross-sections of fixed tissue and calculating the ratio of diseased to healthy tissue. (B) Collagen content of various cavity morphologies, assessed by trichrome staining and H&E. Mean & SD. (C) Collagen content of lesions of various ages as assessed by trichrome staining and serial CT scans, respectively. Mean & SD.

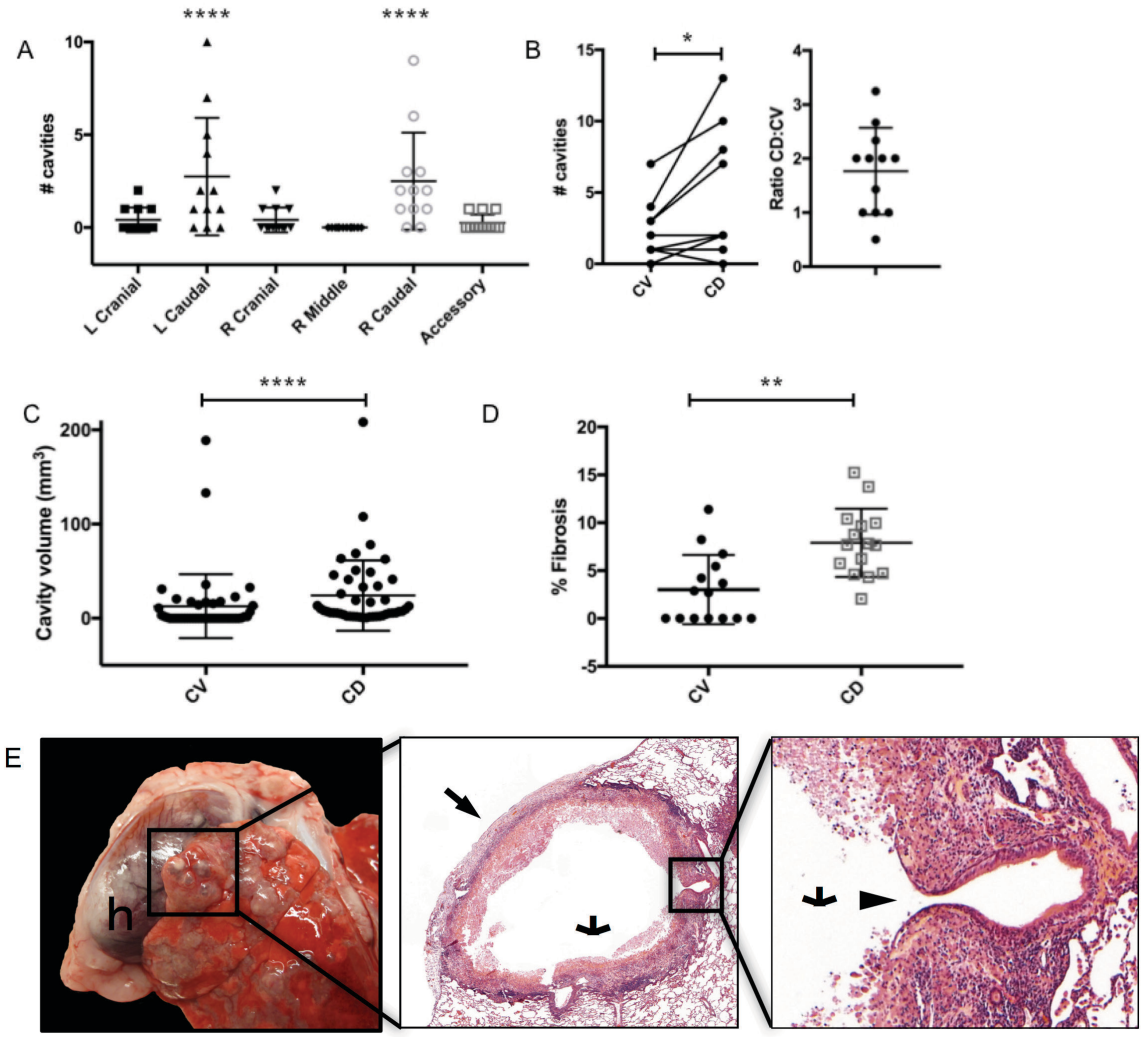

Figure 3.4: Cavities occur at regions of high mechanical stress, where they become larger and more fibrotic.

(A) Distribution of cavities within the lung of TB-infected rabbits, enumerated by CT scan. Each point represents data from a single animal. Significantly more cavities form in the right and left caudal lobes. $p < 0.0001$ (****), one-way ANOVA with Kruskal-Wallis test. Mean & SD. (B) Cavities preferentially form in the caudodorsal lung fields (CD) when compared to cranioventral lung fields (CV). Connected lines represent cavities in the same animal. $p < 0.05$ (*), Wilcoxon paired t test. Mean and SD. (C) Maximum volumes attained by cavities occurring in the CV or CD lung fields. $p < 0.0001$ (****), Kolmogorov-Smirnov test. Mean and SD. (D) Percentage of the cavity wall composed of fibrotic tissue, calculated by positive trichrome staining (collagen). $p = 0.0025$ (**), Kolmogorov-Smirnov test. Mean and SD. (E) A majority of cavities are subpleural, and are associated with pleural inflammation and fibrosis. Few cavities display histologic evidence of airway communication (h= heart; *= cavity lumen; arrow= pleural surface; arrowhead= airway communication).

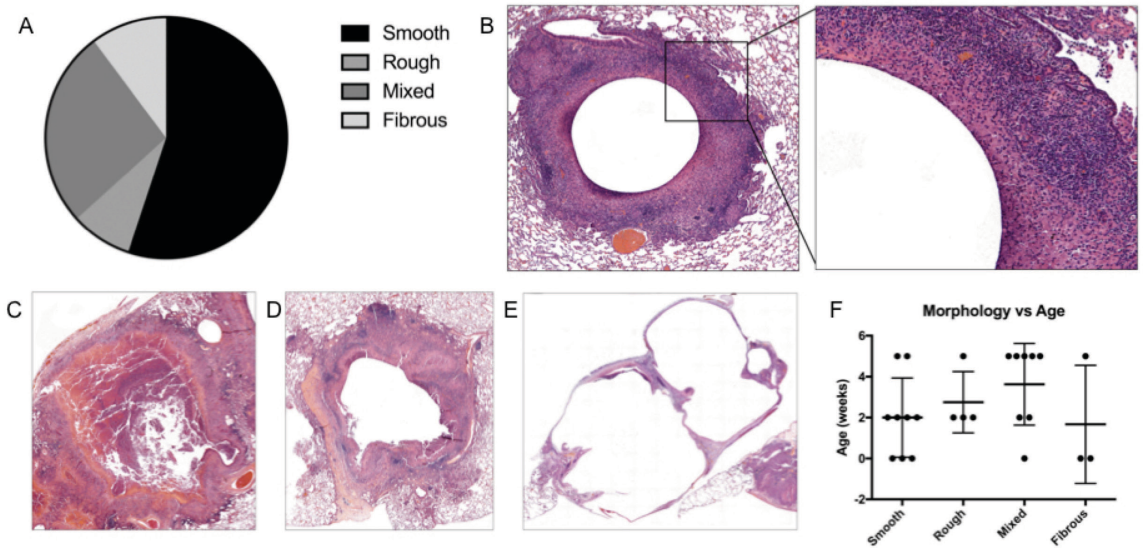

Figure 3.5: Histopathology reveals divergent cavitary morphology.
(A) Histopathologic analysis of 49 cavitary lesions from 20 animals shows four distinct cavitary morphologies. (B) A "smooth" pulmonary cavity with a sharply defined gas-tissue interface, adjacent to a bronchiole. Hematoxylin & eosin (H&E). Inset, higher magnification of interior surface of cavity. (C) A large subpleural cavity with "rough" morphology, associated with focal pleuritis and pleural fibrosis. H&E. (D) A subpleural "mixed" cavity. The upper portion of the cavity has a smooth well-demarcated gas-tissue interface, while the lower portion is rough and ragged. The cavity has partially collapsed, leaving a dense band of fibrosis at the left aspect of the cavity. H&E. (E) A very large "fibrous" or "tension-type" cavity expands and obliterates the tip of a lung lobe, extending to both pleural surfaces. The wall is composed of mature fibrous connective tissue lined by scant necrotic debris and minimal cellular infiltrate. H&E. (F) Age of cavities based on serial CT scans and correlation with terminal histopathology. Mean and SD.

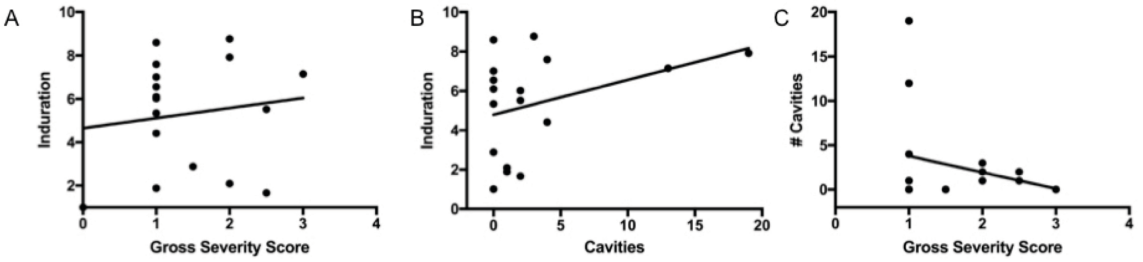

Figure 3.6: Tuberculin reactivity is not predictive of cavitation or disease severity.
(A) Scatter plot of the degree of induration at 48 hours following dermal old tuberculin and gross severity scores based on the percentage of lung affected. Each point represents an individual animal. $R^2 = 0.06$. (B) Degree of induration at 48 hours plotted against number of cavities. $R^2 = 0.13$. (C) Number of cavitary lesions plotted against gross severity scores. Note animals with extensive cavitation but minimal gross pathology. $R^2 = 0.02$. Linear regression with Spearman correlation coefficients and 95 confidence interval showing line of best fit (solid black lines, all plots).

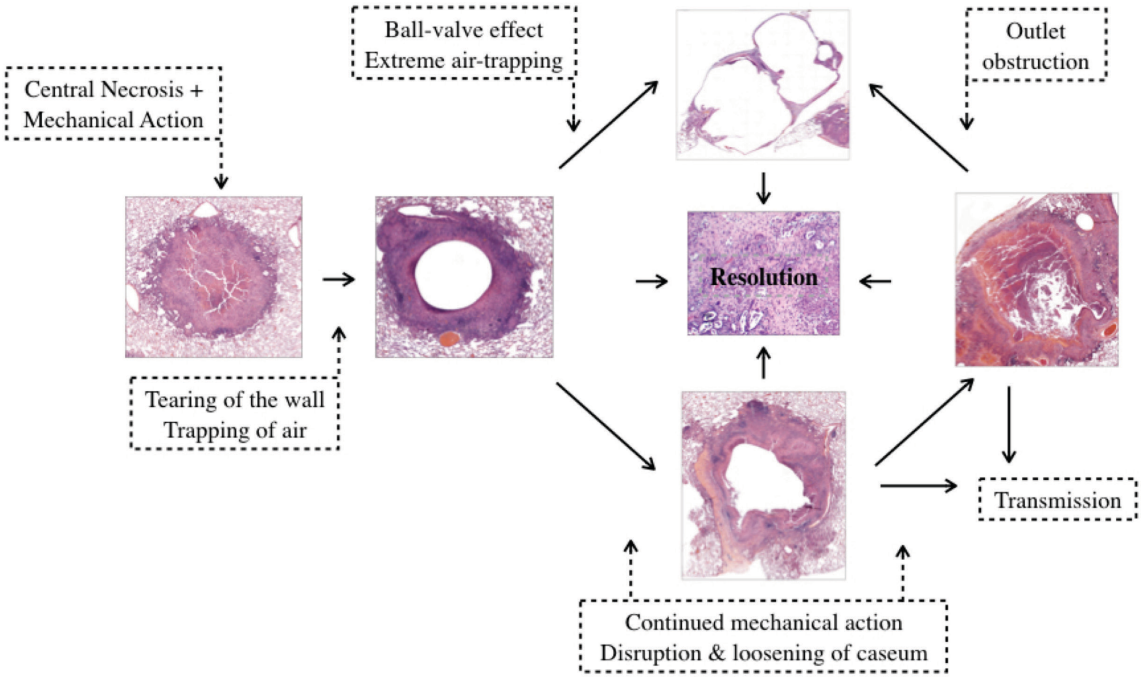

Figure 3.7: Proposed mechanism of cavity genesis and progression.
A cavity begins when mechanical action disrupts the necrotic granuloma by causing a tear in the fibrotic wall. With inspiration, external tension in the surrounding lung tissue pulls air into the necrotic center, causing a smooth cavity. If at any point the outlet is severely obstructed creating a ball-valve effect, extreme air trapping occurs and causes the cavity to assume a thin-walled fibrous balloon-like morphology. If the outlet is open or only partially obstructed, air accumulates less rapidly, resulting in smaller cavities which may progress or wax and wane. The mechanical actions of respiration continue to act on these lesions, causing eventual disruption and loosening of the retained caseum. This newly-freed material is coughed up in the sputum to continue the transmission cycle, leaving behind a mixed or rough cavity with a wall of progressively crumbling caseum. Finally, any of these lesions may spontaneously close and resolve, leaving a residual scar.

Chapter 4

Mycobacterium Tuberculosis Induces Necroptosis in a Mouse Model of Necrotizing and Cavitary TB.

4.1 Abstract

Mycobacterium tuberculosis (MTB) manipulates host cell death pathways to complete its life cycle. Necrosis, a pro-inflammatory form of cell death, increases TB-associated mortality by driving tissue destruction, antibiotic resistance and bacterial transmission. *In vitro* studies suggest that MTB exploits Receptor Interacting Protein (RIP) kinases to initiate host cell necroptosis – a form of programmed cell death - but translating these findings to animal models has been challenging, and the role of RIP kinases *in vivo* has been insufficiently explored. In the current study, C3HeB/FeJ mice

were infected aerogenously with 1.6 $\log_{10}$ colony forming units (CFU) of virulent MTB, and then received a novel RIP1 kinase inhibitor (GSK'547) delivered in chow, or nutritionally equivalent control chow from week 3 to 11 post-infection. Animals were sacrificed at two-week intervals for quantification of CFU, lung and serum cytokines, and immunohistopathology. Immunostaining for pMLKL – the final executioner of necroptosis – was strongly positive in macrophages within and around granulomas, confirming that necroptosis plays an important role during *in vivo* MTB infection. However, GSK'547 did not result in a reduction in pMLKL staining in treated animals. CFU counts, cytokines, and pathology also did not differ significantly between groups. These results confirm *in vitro* observations that necroptosis is induced by MTB during infection, but suggest that its induction may involve bypass of RIP1 kinase.

4.2 Introduction

The pathologic hallmark of MTB infection is the caseating granuloma, which is composed of a core of necrotic debris surrounded by layers of heterogeneous inflammatory cells and contained within a fibrotic capsule [26]. Necrotic debris provides a rich bacterial growth medium which doubles as a barrier to antibiotic penetration, contributing to antibiotic resistance and treatment failure [72,73]. Additionally, necrotic cell death is pro-inflammatory, releasing numerous chemical mediators that stimulate additional inflammation [74]. This over-amplification of the immune response causes the bulk of TB-associated morbidity and pathology [75]. Necrosis is also a prerequisite for the development of pulmonary cavities, the air-filled spaces left behind when a caseating

granuloma discharges its contents into an airway [26]. As discussed in previous chapters, cavitation is the principle means of bacterial transmission, and has been identified as an independent risk factor for the emergence of drug resistant TB strains [6,7]. Despite the immense importance of necrosis in the continued spread of TB, little is known about the pathways through which host necrosis occurs. Until very recently, necrosis was thought to be a disordered, unregulated, and unavoidable consequence of active infection. Necroptosis, a newly discovered form of programmed necrosis executed by RIP kinases, has immense implications for TB control. Multiple lines of evidence now suggest that MTB exploits RIP kinases to induce host necrosis [76–79]. Thus, inhibition of RIP kinases has the potential to block this tissue destruction. Adjunctive therapies that inhibit host necrosis will lessen the global TB burden by reducing transmission, treatment failure, and antimicrobial resistance.

4.3 Host cell death during MTB infection

MTB is an obligate intracellular parasite that manipulates host cell death pathways to survive and propagate. Cells infected with MTB may undergo death by apoptosis or necrosis, a key divergence between attenuated and virulent TB strains [77]. Apoptosis, a form of programmed cellular suicide, serves a host-protective role during TB infection by eliminating infected cells without triggering additional inflammation. Cells neatly package their disassembled contents into apoptotic bodies, which are then consumed by phagocytic cells. Apoptosis is most strongly induced by avirulent strains such as H37Ra, favoring bacterial control [77]. Conversely, death by necrosis is lytic and messy, resulting in

uncontrolled release of cellular contents and infectious bacteria, both of which stimulate additional inflammation and tissue destruction [31]. Although the ability to induce host cell necrosis is a defining characteristic of virulent MTB [80], little is known about the specific host mechanisms through which necrosis is induced or executed.

The pro-inflammatory cytokine TNFα has been conclusively linked to necrosis during TB infection [81]. TNFα is required for early bacterial control, and TNFα deficiency results in host cell necrosis due to overwhelming bacterial proliferation [82]. However, high TNFα also results in host necrosis despite adequate control of bacterial growth, implicating TNFα as a major driver of TB immunopathology [76,81]. Due to the serious risks of immunosuppression and disease reactivation during latent TB infection (LTBI), TNFα inhibition is not a viable strategy for adjunctive therapy during TB in human patients [83]. However, the recent discovery of necroptosis, a form of programmed necrosis canonically induced by TNFα, has immense implications as the critical missing link between high TNFα and host necrosis during TB infection [84].

Necroptosis is triggered in cells when apoptosis is stimulated while simultaneously blocked at a downstream checkpoint [85]. This pathway was initially identified as a backup suicide mechanism for cells infected with viruses encoding caspase inhibitors, such as Herpesvirus [86]. Other intracellular bacteria, including *Listeria monocytogenes* and *Francisella tularensis* also exploit the necroptotic pathway as a virulence strategy [87]. Canonically, activation of necroptosis involves death receptor engagement by TNFα in the face of caspase inhibition, leading to the formation of a "necrosome" catalyzed by RIP1 and composed of multiple RIP3 subunits and the effector molecule MLKL (Figure

4.1) [88]. Noncanonical activation occurs by interferon (IFN) stimulation, or through engagement of pattern recognition receptors (PRRs) such as TLR3/4 or DAI [89]. Activation of the necrosome ultimately leads to cellular and nuclear membrane disruption, release of reactive oxygen species (ROS) and necrotic cell death [89]. MTB produces multiple known apoptotic inhibitors (Figure 4.1) [90], and it is likely that virulent TB strains exploit necroptosis as a means of dissemination. *In vitro* studies in mouse and human macrophages have demonstrated that treatment with the RIP1 inhibitor Necrostatin-1s protects from necrotic cell death [78]. However, translating these findings to *in vivo* models has been challenging [78].

Recently, Roca *et al.* demonstrated that knock-down of RIP1 or RIP3 in Zebrafish infected with *Mycobacterium marinum* (a model system for examining the innate response to mycobacterial infection) leads to decreased bacterial burdens and reduced extracellular bacteria, further supporting the involvement of necroptosis in mycobacterial dissemination. They also demonstrated that pharmacologic inhibition of RIP1 achieves similar protection, teasing the possibility of necroptosis inhibitors as future adjunctive therapy for tuberculosis [76]. Although overt histopathologic necrosis is not a feature of MTB infection in most mouse strains [91], studies by Zhao *et al.* revealed that *RIP3-/-* mice infected with *M. tuberculosis* exhibit reduced CFU counts when compared to wild type (WT) mice. This phenotype was shown to be transferrable by transplantation of *RIP3-/-* alveolar macrophages to immune-deficient mice [77]. Despite mounting evidence that necroptosis impairs control of TB, the critical role of RIP1, the key decision checkpoint

and initiator of the necroptosis complex, has not been explored during *in vivo* MTB infection.

Elucidation of the role of RIP1 *in vivo* has been hindered by a lack of genetic tools, with *RIP1-/-* mice dying shortly after birth [92]. As different cell types display widely differential susceptibility to necroptosis induction [78,93], conditional or tissue-specific knockout animals are likely to underestimate the effects of necroptosis in inflammation and tissue destruction. Although a handful of RIP1 inhibitors have recently been made commercially available, these drugs exhibit significant off-target effects and poor pharmacokinetic properties, making them unsuitable for long-term *in vivo* dosing [94].

4.4 Mouse models of necrotizing pulmonary TB

Until recently, mice have been overlooked as models of necrotizing pulmonary TB, since commonly used mouse strains do not form the caseating granulomas characteristic of the infection in humans [91]. However, immunocompetent C3HeB/FeJ mice develop highly organized, encapsulated hypoxic and necrotic lesions following TB infection [28,95]. Importantly, these lesions are much more representative of the observed pathology in human TB patients than those generated by a majority of other mouse strains. TNFα inhibition in conjunction with standard antibiotic therapy results in a significant reduction in both CFU counts and necrotic pathology, confirming TNFα as a major mediator of necrosis in this model [96]. However, due to the serious risk of disease reactivation during latent TB infection (LTBI), TNFα inhibition is not a viable strategy for adjunctive therapy during TB in human patients [82].

The high susceptibility of C3HeB/FeJ mice to TB infection is associated with the "super-susceptibility to tuberculosis-1" (*sst1*) locus on chromosome 1. The *sst1* locus was recently discovered as a key genetic determinant of necrotic pathology in the C3HeB/FeJ mouse, but the exact mechanism through which this occurs is currently unknown [31]. The *sst1* locus contains the newly-identified *IPR1* (intracellular pathogen resistance) gene which is involved in modulating the host response to intracellular stress [30,31]. The mode of death in *sst1*-susceptible macrophages shares many similarities with RIP1-mediated necroptosis (Table 4.1), including substantial overlap in the initiators (TNFα and type I/II IFNs), mediators (JNK, PKR), and executioners (reactive oxygen species [ROS], mitochondrial permeability) [32,85]. Interestingly, *sst1*-susceptible cells are also hypersusceptible to *Listeria monocytogenes* and *Francisella tulirensis*, two bacterial pathogens which also exploit necroptosis as a mechanism of virulence [87]. As with necroptosis, blockage of sst1-mediated necrosis shifts cells to apoptotic death [32]. We hypothesize that *IPR* acts as a brake on necroptosis during MTB infection, and that pharmacologic inhibition of RIP1 will alleviate necrosis in this model.

	Sst1-mediated death	RIP1-mediated death
Induction	TNFα Type I, II IFN	TNFα (canonical) Type I, II, IFN, TLR3/4, DAI, etc. (noncanonical)
Mediators	ROS	RIP1, RIP3, MLKL, ROS
Inhibition	IFNR > TNFR blockers PKR inhibitors JNK inhibitors ROS scavengers	Necrostatins GSK'547 PKR inhibitors JNK inhibitors ROS scavengers
Morphology	Mitochondrial disruption, necrosis	Mitochondrial disruption, necrosis

Table 4.1: There is extensive overlap between RIP1-mediated and *sst1*-mediated necrosis. Both result in necrotic cell death as a result of mitochondrial membrane disruption and release of reactive oxygen species (ROS). Multiple initiators and mediators are shared between the two pathways. Finally, inhibition of both *sst1* and RIP1-mediated necrosis results in a shift from necrotic to apoptotic death.

4.5 Methods

Mouse infection. 140 female C3HeB/FeJ mice (Jackson Labs, Bar Harbor ME) were obtained at 6-8 weeks of age and allowed to rest for one week after introduction to the facility. Animals were grouped housed under Biosafety level 3 conditions in accordance with protocols approved by the Institutional Animal Care and Use Committee at Johns Hopkins University (Baltimore, MD, USA). Mice were infected directly from a frozen stock of *Mycobacterium tuberculosis* H37Rv using an aerosolization system (Glas-Col Inc., Terre Haute, IN, USA). Animals in one cohort received GSK'547 formulated into chow from weeks 3-11 post infection, while those in the control cohort received equivalent non-medicated chow (Purina Research Diets, New Brunswick NJ, USA). Animals were weighed weekly to assess for disease-related weight loss.

CFU and cytokine determination. Six mice were sacrificed on day one post-infection for enumeration of implantation colony forming units (CFU). For CFU counts, lungs and spleens were isolated and ground into a homogenate before being serially diluted and grown on 7H11 selective agar (Becton Dickinson, Franklin Lakes, NJ, USA) for a minimum of three weeks. Blood and bronchoalveolar lavage fluid (BALF) were collected immediately post-mortem. Blood was collected via cardiac puncture and allowed to clot at room temperature before centrifugation. BALF was collected by instilling 500 ul of sterile PBS into the cervical trachea, followed by syringe aspiration of the instilled fluid. This was repeated once, resulting in 1mL total volume lavage fluid per lung. Lungs used for BALF collection were used exclusively for histopathology, and not for CFU determination. Serum and BALF were passed through a 0.22 um PES syringe

filter (Thermo Scientific, Waltham, MA, USA) to remove Mycobacteria. IL-1beta, IL-2, IL-6, IL-10, IL-12, TNF alpha, and IFN gamma were quantified using the Bio-Plex Pro Mouse Cytokine Th1 Panel (Bio-Rad, Hercules CA, USA). IFN-beta concentrations were determined using the Mouse IFN-beta Quantikine ELISA (R&D systems, Minneapolis, MN, USA).

Histopathology & immunofluorescence. Following sacrifice, lungs were instilled with 600-800 ul of 10% neutral buffered formalin (NBF) before fixation. After 48 hours of fixation, lungs were processed and paraffin-embedded whole, cut into 5 um coronal sections and stained with hematoxylin and eosin (H&E), or processed for immunofluorescence. Heat-induced epitope retrieval was performed in citrate buffer at pH 6. Blocking with TBST+ 5% normal goat serum was performed prior to permeabilization using .1% Triton X-100 in TBST for 10 minutes. Samples were simultaneously incubated with primary antibodies diluted with TBST+ 5% normal goat serum for 1 hour, followed by incubation with directly-conjugated primary antibody and secondary antibodies diluted with TBST to 2 ug/ml for one hour. Primary antibodies: anti-phospho-MLKL 196436 (Abcam, Cambridge, MA), anti-Vimentin 300-223 (Novus Biologicals, Centennial, CO), anti-CD68 201844 (Abcam, Cambridge, MA). Secondary antibodies: anti-rabbit 175471 (Abcam, Cambridge, MA), anti-chicken 150171 (Abcam, Cambridge, MA). Fluorshield Mounting Medium with DAPI (Abcam, Cambridge, MA) was used for coverslipping and staining. Slides were viewed using a Nikon Eclipse TI confocal microscope with attached Nikon AI camera. Images were compiled and edited in ImageJ (version 1.49, NIH, USA). Stained slides were digitized with Aperio

ScanScope (Leica Biosystems, Buffalo Grove, IL, USA) and analyzed using Aperio Image Scope (v12.3.2.8013, Leica Biosystems, Buffalo Grove, IL, USA).

Minimum Inhibitory Concentration (MIC) of GSK'547. An Alamar Blue viability assay was performed using *M. tuberculosis* H37Rv grown in liquid 7H9. Aliquots of MTB were grown for 7 days in broth culture prior to drug application. GSK'547 was compared to isoniazid (INH) and untreated controls to determine the IC-50.

4.6 Results

The C3HeB/FeJ mouse is a model of necrotizing and cavitary pulmonary tuberculosis. C3H3B/FeJ mice are uniquely susceptible to *Mycobacterium tuberculosis,* and respond to infection by developing extensive pulmonary necrosis. This results in the development of large caseating granulomas characteristic of the disease in humans, but not seen in other commonly used mouse strains [91]. To further characterize the development of necrosis in this model, we infected 140 C3HeB/FeJ mice with virulent MTB via aerosol. Infected mice reliably developed a spectrum of lesions, ranging from macrophage-rich pneumonia to organized granuloma formation, to formation of large caseating necrogranulomas (Figure 4.2A). Cavitation was occasionally seen, always originating within large necrotic lesions. The observation of cavitation in this model further confirms necrosis as a critical event preceding cavitation, as cavitation has not been documented in other rodent models of MTB infection [42,97].

Mycobacterium tuberculosis infection stimulates phosphorylation of MLKL in vitro. To establish if necrosis in this model occurs as a result of RIP-mediated

necroptosis, we infected mice with a low-dose of aerosolized MTB and performed immunofluorescent staining for phosphorylated MLKL (pMLKL), the final effector of necroptosis. Robust phosphorylation of MLKL was seen throughout the lungs of infected mice surrounding large necrotic granulomas (Figure 4.2B) and in regions of macrophage-rich inflammation (Figure 4.2C), with minimal positive staining in regions of histologically normal lung. Staining for CD68 and vimentin was performed simultaneously to determine the cellular compartmentalization of pMLKL. Cytoplasmic aggregates of pMLKL were seen primarily within CD68+ macrophages (Figure 4.2B, 4.2C), and to a lesser extent in vimentin+ fibroblasts and non-labeled cells (not shown).

GSK'547 monotherapy does not protect from MTB-induced pulmonary necrosis. Due to the presence of robust MLKL phosphorylation indicating activation of necroptosis, we hypothesized that inhibition of RIP1 kinase would inhibit necroptosis and alleviate severe lung pathology in this model. RIP1 kinase, the key decision checkpoint downstream of TNFα stimulation, is composed of three domains – a kinase, intermediate, and death domain [92]. While the kinase domain is required for initiation of necroptotic death, it is dispensable for NF□□ generation, making RIP1 an attractive therapeutic target [98]. A handful of well-characterized RIP1 inhibitors have emerged in the past several years, but very few have been utilized in animal models. Necrostatin-1s, the most potent available RIP1 inhibitor, has a short half-life and shows significant off-target effects, making it unsuitable for long-term *in vivo* dosing [94]. Our collaborator Dr. John Bertin has developed GSK'547: a next-generation RIP1 inhibitor that demonstrates superior potency and selectivity over Necrostatin-1s, significantly limiting its off-target

effects. GSK'547 achieves greater than 90% RIP1 inhibition within 24 hours when administered to mice in chow, and is suitable for long-term dosing (data not shown).

To examine the role of RIP1 during *in* vivo TB infection, C3HeB/FeJ mice were infected with a low dose (1.6 log CFU) of aerosolized MTB and treated with the novel RIP1 inhibitor GSK'547 or vehicle control from week 3-11 post infection. Grossly, lungs from treated animals were indistinguishable from controls at weeks 5, 7, 9 and 11 (Figure 4.3A). For microscopic analysis, digital quantification of inflammation and necrosis was performed on H&E stained lung sections. Somewhat surprisingly, these parameters were not improved by GSK'547 treatment. The percentage of affected to unaffected lung tissue was similar in both groups, averaging approximately 30% (Figure 4.3B), while the percentage of necrosis in treated animals was slightly higher on average (Figure 4.3C). We next sought to determine if GSK'547 treatment had any effect on lesion phenotype by measuring the size of both inflammatory and necrotic lesions. Inflammatory lesions varied considerably in size within individual animals, but did not differ between groups (Figure 4.3D). Necrotic foci displayed less variability with the exception of one individual, and were also similar between treated and untreated animals (Figure 4.3E).

GSK'547 does not impact mycobacterial survival. To determine if GSK'547 is able to directly influence mycobacterial survival, a colorimetric cell viability assay was performed, using isoniazid, a first-line antomycobacterial drug as a positive control. We confirmed that GSK'547 lacks antimycobacterial activity *in vitro* at all concentrations tested, up to 64 ug/mL. As host necrosis is known to promote the propagation of MTB *in vivo*, we hypothesized that necrosis inhibition by GSK'547 would indirectly decrease

mycobacterial proliferation. To determine if GSK'547 influences mycobacterial survival *in vivo*, colony forming unit (CFU) counts in the lung and spleen were performed over the course of infection. After 11 weeks, GSK'547 monotherapy had no effect on the bacterial burdens in either the lungs or spleens of infected mice (Figure 4.4A, 4.4B). At the time of sacrifice, spleen weights were measured to serve as an estimate of overall systemic immune activation. Spleen weights were similar between groups at all time points, indicating similar magnitudes of systemic immune activation in both treated an untreated animals (Figure 4.4C). Weight loss was observed in the treatment group at the onset of treatment, but all animals appeared healthy and gained weight appropriately throughout the study (Figure 4.4D), suggesting a palatability issue rather than a direct effect of the drug.

GSK'547 does not significantly alter cytokine profiles of infected mice. The role of RIP1 in necroptosis is dependent on its kinase domain, as phosphorylation and activation of Rip3 by Rip1 promotes downstream MLKL phosphorylation and necrotic cell death (Figure 4.1). However, RIP1 has pleotropic functions, and can also serve a pro-survival role in the cell. During pro-inflammatory signaling, RIP1 is ubiquitinated (multiple domains) and serves a scaffolding function in NFkB generation through the intermediate domain [92]. To examine the effect of RIP1 inhibition on pulmonary and systemic immune responses, cytokines were quantified in both serum and bronchoalveolar lavage fluid (BAL) of infected mice, and then compared to uninfected controls (Figure 4.5). Levels of IFNγ, IL-6, IL-12 and IL-10 did not differ significantly from controls in either BAL fluid or serum. Serum levels of IFNγ, the principle cytokine

of MTB control, decreased in all groups from weeks 7-11 (Figure 4.5A, potentially signaling the onset of the Th1 dysregulation that characterizes severe disease. Cytokine levels overall were higher in BAL samples than in serum, suggesting local pulmonary cytokine concentrations may give a more representative picture of immune status during MTB infection than serum profiling. Total cytokines recovered from BAL fluid were also relatively low, and future analyses may benefit from use of tissue homogenates. Serum and BAL levels of TNFα, IL-1β, IL-2 and IFNβ were below levels of detection at all time points (data not shown).

4.7 Discussion

Necroptosis, mediated by Receptor Interacting Protein (RIP) kinases, has been implicated in the pathogenesis of MTB-induced host cell death *in vitro* [76–78], but appropriate *in vivo* models are currently lacking. We demonstrate for the first time that the C3HeB/FeJ mouse, a recently characterized model of necrotizing and cavitary pulmonary tuberculosis [42], undergoes MTB-induced necroptosis. We observed robust MLKL phosphorylation within pulmonary macrophages of C3HeB/FeJ mice in response to low-dose aerosol MTB infection, confirming the execution of necroptosis in these cells. This contrasts sharply with the findings of Stutz *et al*, who report that MLKL phosphorylation is not a feature of macrophage death *in vivo* using C57B/6 mice[99]. This may reflect an important strain difference, as C57B/6 do not generate necrotic lesions when infected with MTB [91]. Additionally, we observed pMLKL staining to a lesser extent in vimentin+ fibroblasts and unlabeled cells. Consistent with the majority of *in*

vitro data [77,78], this confirms macrophages as the major, but not exclusive cell population to undergo MTB-induced necroptosis during infection.

Having established the C3HeB/FeJ mouse as an *in vivo* model of MTB-induced necroptosis, we next sought to utilize this model to test novel pharmacologic inhibitors of necroptosis. Despite evidence of robust necroptosis activation, the novel RIP1 inhibitor GSK'547 failed to protect mice from necrotic pathology and had no effect on bacterial replication. Although this seems to contradict the established *in* vitro literature, there are several possible explanations for GSK'547's observed lack of effect. Poor penetration of chemotherapeutics into necrotic and fibrotic tuberculous lesions is a problem both in human patients and animal models [72]. Although the concentration of drug administered in this study was chosen to achieve 90% RIP1 inhibition within 24 hours based on PK studies conducted at GlaxoSmithKline, it is possible that drug concentrations did not reach adequate levels in granulomatous tissue due to poor penetration. Future studies will focus on quantifying the amount of drug within lesional tissue in order to confirm adequate drug exposure.

RIP1, required for canonical necroptosis activation, is dispensable in several alternatively activated pathways such as those shown in Figure 4.1 [89]. It is possible that necroptosis activation in MTB-infected macrophages proceeds through one of these alterative pathways. Recently, Niederweis *et al* demonstrated one such RIP1 bypass pathway induced by Tuberculosis Necrotizing Toxin (TNT), an NAD glycohydrolase [79]. TNT, produced by virulent MTB, induces necrosis through host cell NAD depletion, which is sufficient to cause RIP3 and MLKL activation in THP-1 macrophages [79]. Taken

together with our findings, this suggests that MTB is able to activate necroptosis independently of the canonical RIP1-TNF axis. However, induction is likely dependent on host cell type, as demonstrated by Butler *et al,* who showed that RIP1 activation is a feature of *in vivo* macrophage death in many, but not all cell lines infected with MTB [78]. Interestingly, THP-1 macrophages were classified as resistant to TNF/RIP1 induced cell death during infection in these experiments [78].

The last decade has seen an explosion of cell death-related research, resulting in the discovery and characterization of numerous programmed death pathways [84]. As the first to be discovered, RIP-mediated necroptosis remains the most well-characterized, and is considered the prototype of regulated necrosis. However, other novel forms of programmed cell death are still being elaborated. Several of these, including pyroptosis, ferroptosis [100], and ETosis [101] have also been implicated in the pathogenesis of mycobacterial-induced cell death [102]. Significant interactions and redundancies between these and other known pathways are becoming apparent, further complicating our understanding of the host-pathogen relationship during cell death and underscoring the necessity of a multi-modal collaborative approach [102]. Elucidation of the role of RIP1 *in vivo* has been hindered by a lack of genetic tools, with *RIP1-/-* mice dying shortly after birth. Genetically engineered mice (GEMs) expressing catalytically inactive RIP1 have recently been established [103]. Unlike their *RIP1-/-* counterparts, these mutant mice are viable, fertile, and free of background pathology [103]. In the future, these mice will allow us to clarify the role of RIP1 during MTB infection. Additionally, cross breeding of RIP1 kinase-dead mice with other susceptible strains such as the C3HeB/FeJ or the newly

characterized *B6J.C3-sst1*^{C3HeBFeJ}*Krmn* (a resistant C57B/6 mouse bearing the C3HeB/FeJ susceptibility locus) [32] will provide valuable information about the role of RIP1 kinase in the genetic susceptibility to tuberculosis.

In summary, we demonstrate that pulmonary macrophages of C3HeB/FeJ mice undergo robust MLKL phosphorylation during *in vivo* MTB infection – confirming necroptosis execution in these cells. Although the novel RIP1 inhibitor GSK'547 failed to protect from necrotic pathology in this study, the C3HeB/FeJ mouse model provides a valuable tool for investigating novel host-directed therapies. As very few rodent models develop overt necrosis in response to MTB infection [27], the C3HeB/FeJ is essential for clarifying the relationship between MTB and programmed cell death pathways.

Figures

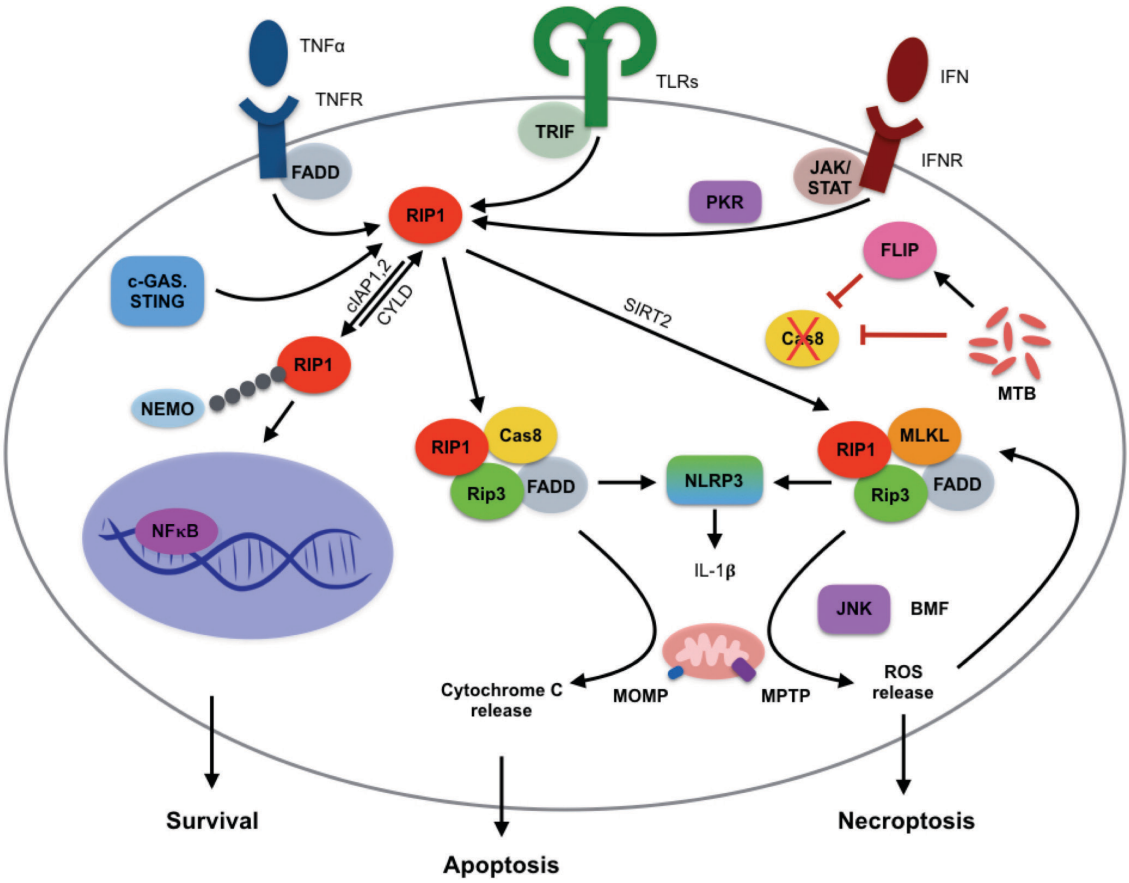

Figure 4.1: Interactions between MTB and the necroptotic pathway.
RIP1 is the key decision checkpoint regulating cell death downstream of TNFα. Outcomes are highly context-dependent, and include 1) cell survival through ubiquitination of RIP1 and transcription of NFkB, 2) apoptosis through Caspase 8 activation and RIP1/RIP3 inactivation, and 3) necroptosis through inactivation of Caspase 8 and formation of the necrosome catalyzed by active RIP1. MTB employs multiple strategies to block apoptosis and promote necroptosis. These include production of soluble TNFα inhibitors, inhibition of caspase 8 at the level of transcription or expression, and induction of FLIP, an anti-apoptotic host protein.

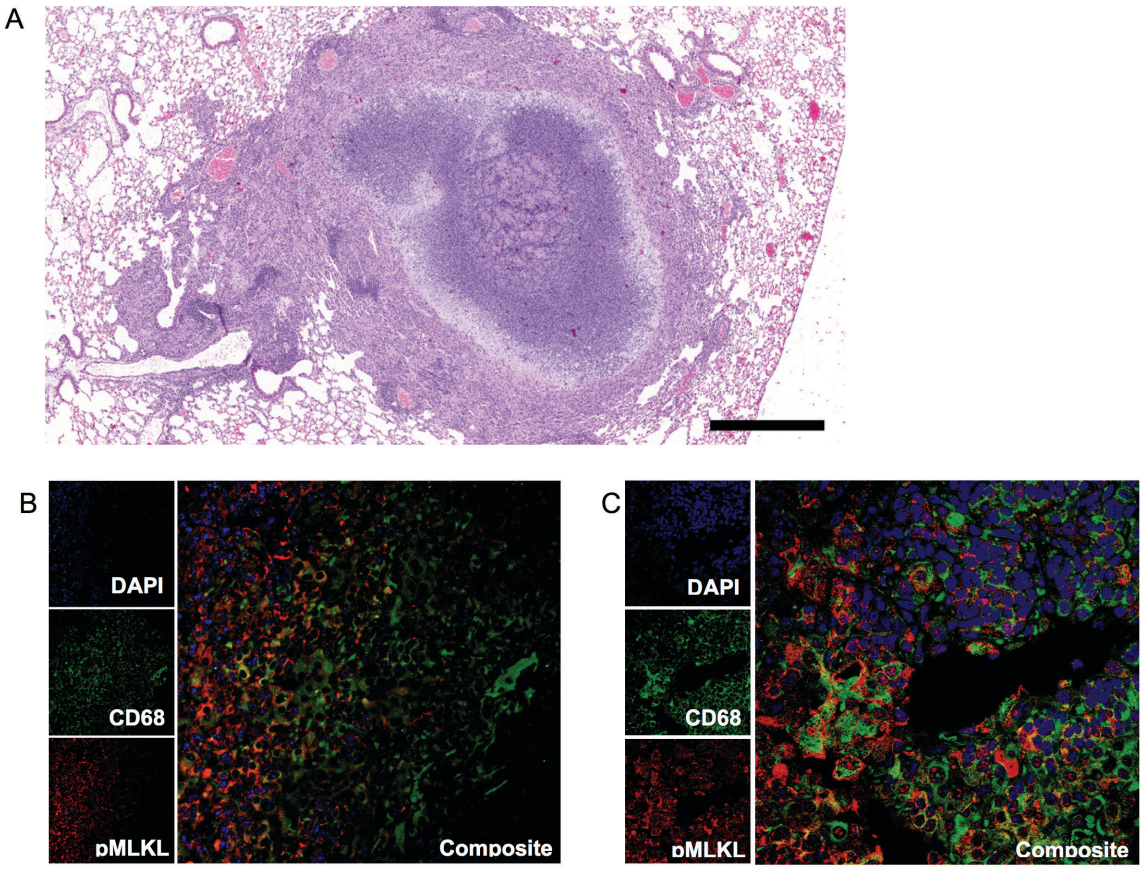

Figure 4.2: MTB infection stimulates pulmonary necroptosis in C3HeB/FeJ mice.
(A) A single large necrogranuloma in the lung of an infected C3HeB/FeJ mouse, typical of lesions in this strain. (B) C3HeB/FeJ mice infected with a low dose of MTB (1.6 log CFU) show strong positive cytoplasmic immunostaining for phosphorylated MLKL in CD68-positive macrophages surrounding necrotic granulomas. The necrotic center is in the lower right corner of the image. 40x. (C) Robust cytoplasmic pMLKL staining in region of macrophage-rich inflammation, surrounding a small respiratory bronchiole. 60x.

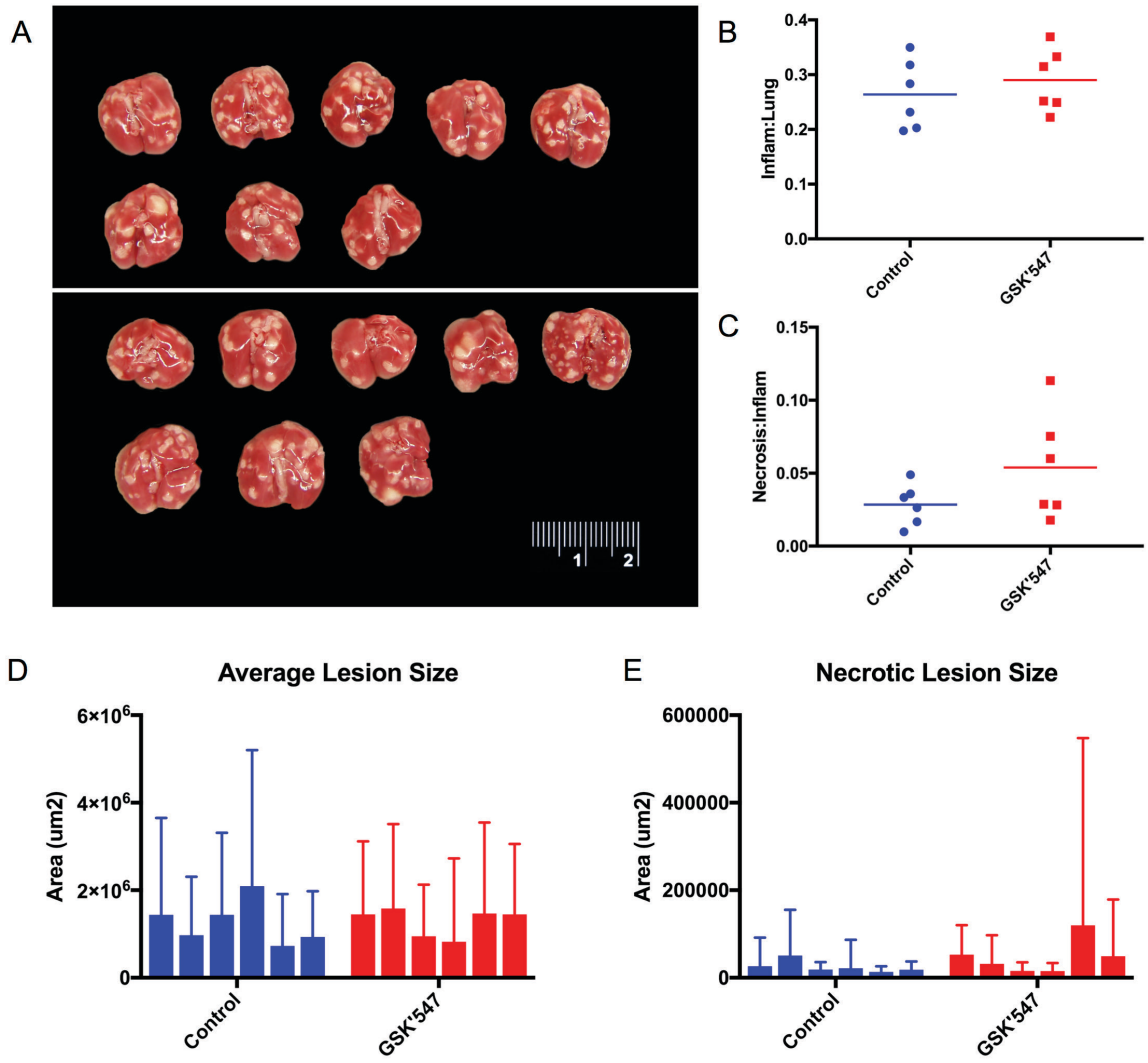

Figure 4.3: The novel RIP1 inhibitor GSK'547 does not protect from MTB-induced necrotic lung pathology in C3HeB/FeJ mice.
(A) Gross photographs of mouse lungs at week 11 post-infection. C3HeB/FeJ mice generate large caseating granulomas which are grossly visible as white/tan foci. Gross pathology is indistinguishable between vehicle-treated (top) and GSK'547-treated animals (bottom). (B) Digital quantitation of lung inflammation as a percentage of total section area on H&E at week 9 post-infection. (C) Digital quantification of lung necrosis, shown as a percentage of inflammation on H&E at week 9 post-infection. There is trend toward increased necrosis in treated animals. (D) Average size of inflammatory lesions in C3HeB/FeJ mice. Each bar represents data from a single animal. (E) Average size of necrotic lesions in C3HeB/FeJ mice. Each bar represents data from a single animal.

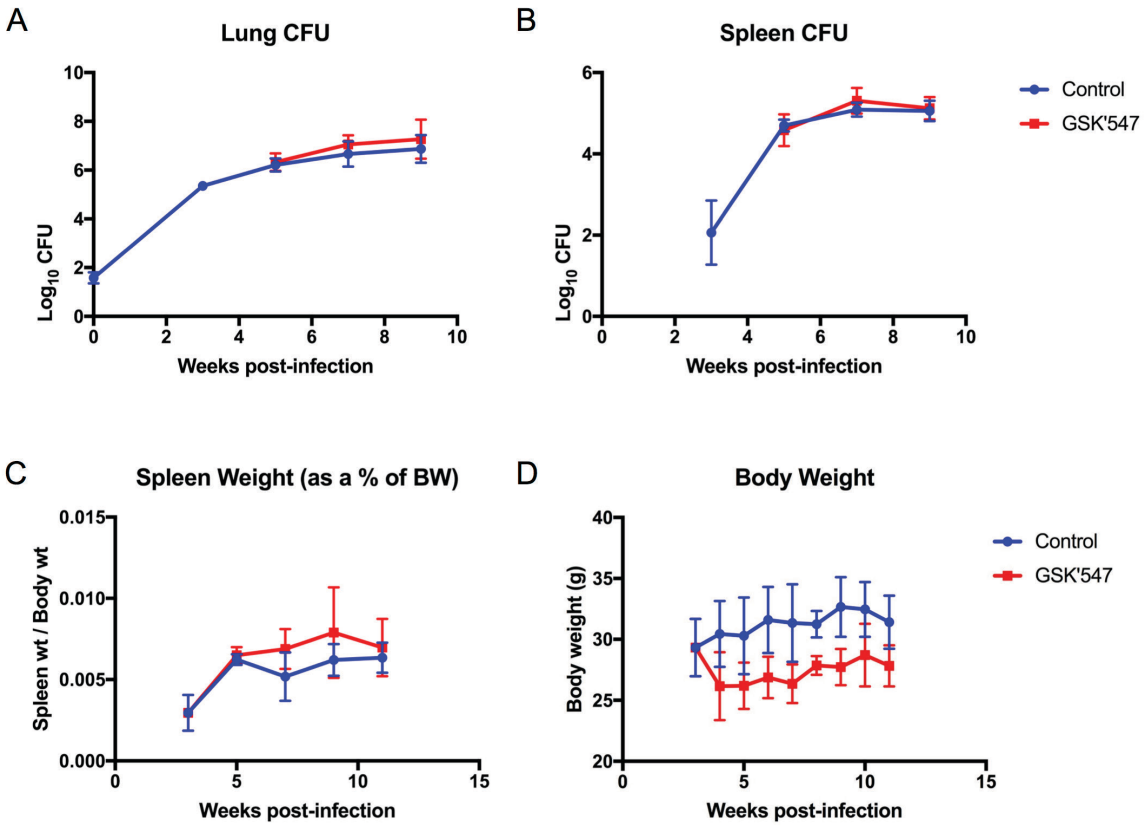

Figure 4.4: GSK'547 treatment does not impact mycobacterial survival in vivo.
(A) Bacterial burden in the lungs of infected animals, shown as the number of colony forming units (CFU). Mean and SD. (B) Bacterial burden in the spleens of infected animals. Mean and SD. (C) Terminal spleen weights as an estimation of systemic immune activation. Due to differences in body weight, spleen weight was normalized to body weight for each animal. Mean and SD. (D) Body weights over the course of infection in treated vs control animals.

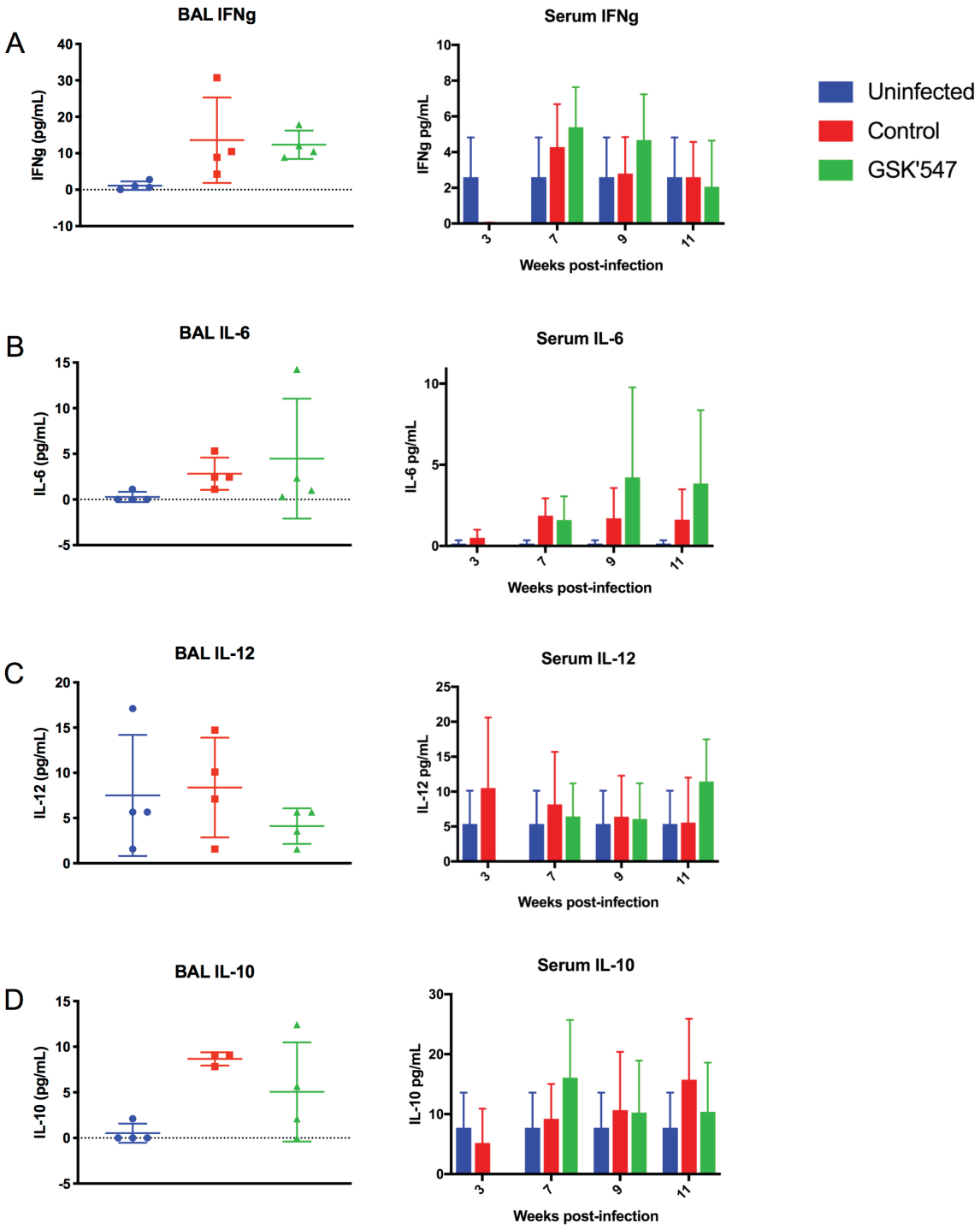

Figure 4.5: Local and systemic cytokine profiles during MTB infection.
Quantification of cytokines from bronchoalveolar lavage (BAL) fluid of C3HeB/FeJ mice at week 9 post-infection, and serum at weeks 3, 7, 9 and 11 post-infection.

Appendix

Abbreviations

AUC .....Area under the curve
BAL, BALF .....Bronchoalveolar lavage fluid
BCG .....Bacillus Calmette-Guérin
BMI .....Body mass index
BSL# .....Bio-safety Level
CD .....Caudodorsal
CD# .....Cluster of differentiation
CFU .....Colony forming units
Cmax .....Concentration maximum
CMI .....Cell Mediated Immunity
CT .....Computed tomography
CV .....Cranioventral
DTH .....Delayed type hypersensitivity
ECM .....Extracellular matrix
EDTA .....Ethylenediaminetetraacetic acid

GEM.....Genetically engineered mice

H&E .....Hematoxylin and Eosin

HDT .....Host-directed therapy

HIV .....Human Immunodeficiency Virus

HU.....Hounsfield units

IC50.....Half maximal inhibitory concentration

IFN .....Interferon

IGRA.....Interferon Gamma Release Assay

IL#.....Interleukin

IM.....Intramuscular

INH .....Isoniazid

IPR .....Intracellular pathogen resistance gene

IV .....Intravenous

LC/MS-MS .....Liquid chromatography/Tandem mass spectrometry

LTBI.....Latent TB infection

MIC .....Minimum inhibitory concentration

MLKL .....Mixed Lineage Kinase-Like Protein

MMP# .....Matrix metalloproteinase

MTB.....Mycobacterium tuberculosis

NBF.....Neutral buffered formalin

NHP.....Non-human primate

NZW .....New Zealand White

OD.....Optical density

PI.....Post infection

PK .....Pharmacokinetic

pMLKL .....Phosphorylated MLKL

PPD .....Purified protein derivative

PPE.....Personal protective equipment

PRR.....Pattern recognition receptor

RIP, RIPK .....Receptor Interacting Protein Kinase

ROI.....Region of interest

ROS.....Reactive Oxygen Species

sst1 .....Super susceptibility to tuberculosis-1 locus

TB .....Tuberculosis

Th# .....T helper

Tmax .....Time maximum

TNFa .....Tumor necrosis factor alpha

TNT.....Tuberculosis necrotizing toxin

TPP.....Transpulmonary pressure

V:Q.....Ventilation to perfusion ratio

WT .....Wild type

References

1. Lougheed, K. *Catching Breath*. (Bloomsbury Sigma, 2017).
2. *Tuberculosis 2007: From Basic Science to Patient Care*. (Bourcillier Kamps, 2007).
3. WHO. Tuberculosis Report 2016. ISBN 978-9241565394.
4. Unaids. *Fact sheet - Latest global and regional statistics on the status of the AIDS epidemic*. at www.unaids.org/sites/default/files/media_asset/UNAIDS_FactSheet_en.pdf
5. Benator, D. *et al.* Rifapentine and isoniazid once a week versus rifampicin and isoniazid twice a week for treatment of drug-susceptible pulmonary tuberculosis in HIV-negative patients: A randomised clinical trial. *Lancet* **360,** 528–534 (2002).
6. Gillespie, S. H. Evolution of drug resistance in Mycobacterium tuberculosis: clinical and molecular perspective. *Antimicrob. Agents Chemother.* **46,** 267–74 (2002).
7. Wallis, R. S. & Hafner, R. Advancing host-directed therapy for tuberculosis. *Nat. Rev. Immunol.* **15,** 255–263 (2015).
8. Perrin, F. M. R. *et al.* Radiological cavitation, sputum mycobacterial load and treatment response in pulmonary tuberculosis. *Int. J. Tuberc. Lung Dis.* **14,** 1596–1602 (2010).
9. Salgame, P., Geadas, C., Collins, L., Jones-López, E. & Ellner, J. J. Latent tuberculosis infection – Revisiting and revising concepts. *Tuberculosis* **95,** 373–384 (2015).
10. Behr, M. A., Edelstein, P. H. & Ramakrishnan, L. Revisiting the timetable of tuberculosis. *BMJ* **362,** 2738 (2018).
11. Rich, A. R. *The Pathogenesis of Tuberculosis.* (Blackwell Scientific Publications.,

1951).

12. Canetti, G. *Thé Tubercle Bacillus in the Pulmonary Lesion of Man.* (Springer International Publishing, 1955).

13. Helke, K. L., Mankowski, J. L. & Manabe, Y. C. Animal models of cavitation in pulmonary tuberculosis. *Tuberculosis* **86,** 337–348 (2006).

14. Leong, F. J., Dartois, V. & Dick, T. *A color atlas of comparative pathology of pulmonary tuberculosis*. (CRC Press, 2010).

15. Lurie, M. B., Abramson, S. & Heppleston, A. G. On the response of genetically resistant and susceptible rabbits to the quantitative inhalation of human type tubercle bacilli and the nature of resistance to tuberculosis. *J. Exp. Med.* **95,** 119–34 (1952).

16. Wells, W. F. & Lurie, M. B. Experimental Airborne Disease. *Am. J. Epidemiol.* **34,** 21–40 (1941).

17. Converse, P. J. *et al.* Pulmonary Bovine-Type Tuberculosis in Rabbits: Bacillary Virulence, Inhaled Dose Effects, Tuberculin Sensitivity, and Mycobacterium vaccae Immunotherapy. *Clin. Diagn. Lab. Immunol.* **5,** 871–881 (1998).

18. Dannenberg, A. M. J. Pathogenesis of human pulmonary tuberculosis: insights from the rabbit model. *American Society of Microbiology, (2014)*.

19. Zachary, J. F. *Pathologic Basis of Veterinary Disease, 6th Edition*. ISBN 978-0323357753.

20. Nedeltchev, G. G. *et al.* Extrapulmonary dissemination of mycobacterium bovis but not mycobacterium tuberculosis in a bronchoscopic rabbit model of cavitary tuberculosis. *Infect. Immun.* **77,** 598–603 (2009).

21. Gadkowski, L. B. & Stout, J. E. Cavitary pulmonary disease. *Clin. Microbiol. Rev.* **21,** 305–333 (2008).

22. Kubler, A. Development and Investigation of a Rabbit Model of Tuberculosis Tissue Destruction. (Imperial College London, 2013).

23. Kübler, A. *et al.* Mycobacterium tuberculosis dysregulates MMP/TIMP balance to drive rapid cavitation and unrestrained bacterial proliferation. *J. Pathol.* **235,** 431–444 (2015).

24. Kubler, A. *et al.* Cathepsin K Contributes to Cavitation and Collagen Turnover in Pulmonary Tuberculosis. *J. Infect. Dis.* **213,** 618–627 (2016).

25. Urbanowski, M. E. *et al.* Repetitive Aerosol Exposure Promotes Cavitary Tuberculosis and Enables Screening for Targeted Inhibitors of Extensive Lung Destruction. *J. Infect. Dis.* **218,** 53–63 (2018).

26. Ihms, E. A., Urbanowski, M. E. & Bishai, W. R. Diverse Cavity Types and Evidence that Mechanical Action on the Necrotic Granuloma Drives Tuberculous Cavitation. *Am. J. Pathol.* **188,** (2018).

27. Kramnik, I. & Beamer, G. Mouse models of human TB pathology: roles in the analysis of necrosis and the development of host-directed therapies. *Semin. Immunopathol.* **38,** 221–237 (2016).

28. Driver, E. R. *et al.* Evaluation of a mouse model of necrotic granuloma formation using C3HeB/FeJ mice for testing of drugs against Mycobacterium tuberculosis. *Antimicrob. Agents Chemother.* **56,** 3181–95 (2012).

29. Ordonez, A. A. *et al.* Mouse model of pulmonary cavitary tuberculosis and expression of matrix metalloproteinase-9. *Dis. Model. Mech.* **9,** 779–88 (2016).

30. Pan, H. *et al.* Ipr1 gene mediates innate immunity to tuberculosis. *Nature* **434,** 767–772 (2005).

31. Pichugin, A. V., Yan, B.-S., Sloutsky, A., Kobzik, L. & Kramnik, I. Dominant Role of the sst1 Locus in Pathogenesis of Necrotizing Lung Granulomas during Chronic Tuberculosis Infection and Reactivation in Genetically Resistant Hosts. *Am. J. Pathol.* **174,** 2190–2201 (2009).

32. Bhattacharya, B. Xiao S, Urbanowski ME, Ordonez A, Ihms EA, Chattrerjee S, Berland R, Pichugin A, Gao Y, Connor J, Ivanov A, Yan B, Kobzik L, Jain S, Bishai WR, Kramnik I. Increased susceptibility to intracellular bacteria and immunopathology driven by a dysregulated macrophage response to TNF. (*Nature Medicine, under revision 2018*).

33. Agostoni, E. Mechanics of the Pleural Space. *Physiol. Rev.* (1972).

34. Seah, G. T., Scott, G. M. & Rook, G. A. W. Type 2 Cytokine Gene Activation and Its Relationship to Extent of Disease in Patients with Tuberculosis. *J. Infect. Dis.* **181,** 385–389 (2000).

35. van Crevel, R. *et al.* Increased Production of Interleukin 4 by $CD4^+$ and $CD8^+$ T Cells from Patients with Tuberculosis Is Related to the Presence of Pulmonary Cavities. *J. Infect. Dis.* **181,** 1194–1197 (2000).

36. Condos, R., Rom, W. N., Liu, Y. M. & Schluger, N. W. Local Immune Responses Correlate with Presentation and Outcome in Tuberculosis. *Am. J. Respir. Crit. Care Med.* **157,** 729–735 (1998).

37. Marakalala, M. J. *et al.* Inflammatory signaling in human tuberculosis granulomas is spatially organized. *Nat. Med.* (2016).

38. Kaplan, G. *et al.* Mycobacterium tuberculosis growth at the cavity surface: a microenvironment with failed immunity. *Infect. Immun.* **71,** 7099–108 (2003).

39. Elkington, P. T., Ugarte-Gil, C. a. & Friedland, J. S. Matrix metalloproteinases in tuberculosis. *Eur. Respir. J.* **38,** 456–464 (2011).

40. Elkington, P. *et al.* MMP-1 drives immunopathology in human tuberculosis and transgenic mice. *J. Clin. Invest.* **121,** 1827–33 (2011).

41. Elkington, P. T., D'Armiento, J. M. & Friedland, J. S. Tuberculosis

immunopathology: the neglected role of extracellular matrix destruction. *Sci. Transl. Med.* **3,** 71ps6 (2011).

42. Ordonez, A. A. *et al.* Mouse model of pulmonary cavitary tuberculosis and expression of matrix metalloproteinase-9. *Dis. Model. Mech.* **9,** 779–788 (2016).

43. Walker, N. F. *et al.* Matrix Degradation in Human Immunodeficiency Virus Type 1–Associated Tuberculosis and Tuberculosis Immune Reconstitution Inflammatory Syndrome: A Prospective Observational Study. *Clin. Infect. Dis.* **86,** 913–22 (2017).

44. Walker, N. F. *et al.* Doxycycline and HIV infection suppress tuberculosis-induced matrix metalloproteinases. *Am. J. Respir. Crit. Care Med.* **185,** 989–997 (2012).

45. Ordonez, A. A. Personal Communication. (2017).

46. Haapanen, J. H., Kass, I., Gensini, G. & Middlebrook, G. Studies on the gaseous content of tuberculous cavities. *Am. Rev. Respir. Dis.* **80,** 1–5 (1959).

47. Coryllos, P. N. & Ornstein, G. G. Giant Tuberculous cavities of the lung. *J. Thorac. Surg.* **8,** 1010 (1938).

48. Belton, M. *et al.* Hypoxia and tissue destruction in pulmonary TB. *Thorax* **71,** 1145–1153 (2016).

49. Hunter, R. L., Olsen, M. R., Jagannath, C. & Actor, J. K. Multiple roles of cord factor in the pathogenesis of primary, secondary, and cavitary tuberculosis, including a revised description of the pathology of secondary disease. *Ann. Clin. Lab. Sci.* **36,** 371–86 (2006).

50. Hunter, R. L. On the pathogenesis of post primary tuberculosis: The role of bronchial obstruction in the pathogenesis of cavities. *Tuberculosis* **91,** S6–S10 (2011).

51. Gekler, W., Lovelace, W., Rankin, H. & Weigel, B. Tuberculous cavitation of the lung: Mechanical factors in its genesis, and combined chemotherapeutic and surgical treatment. *JAMA* **82,** 457–463 (1924).

52. Coryllos, P. N. The mechanics and biology of tuberculous cavities. *Am. Rev. Tuberc* (1935).

53. Coryllos, P. N. Physics Applied to Tuberculosis. *J. Franklin Inst.* **227,** 287–304 (1939).

54. Eloesser, L. Blocked Cavities in Pulmonary Tuberculosis. *J. Thorac. Surg.* **7,** 1–22 (1937).

55. MEDLAR, E. M. The behavior of pulmonary tuberculous lesions; a pathological study. *Am. Rev. Tuberc.* **71,** 1–244 (1955).

56. West, J. B. Distribution of mechanical stress in the lung, a possible factor in localization of pulmonary disease. *Lancet* **297,** 839–841 (1971).

57. Casha, A. R. *et al.* A hypothesis for reactivation of pulmonary tuberculosis: How

thoracic wall shape affects the epidemiology of tuberculosis. *Clin. Anat.* **28,** 614–620 (2015).

58. Cardona, P.-J. A spotlight on liquefaction: evidence from clinical settings and experimental models in tuberculosis. *Clin. Dev. Immunol.* **2011,** 868246 (2011).

59. D'Angelo, E., Bonanni, M. V., Michelini, S. & Agostoni, E. Topography of the pleural surface pressure in rabbits and dogs. *Respir. Physiol.* **8,** 204–229 (1970).

60. Wagner, P. D., Laravuso, R. B., Umm, R. R. & Wesm, J. B. Continuous Distributions of Ventilation-Perfusion Ratios in Normal Subjects Breathing Air and 100% 02. *J. Clin. Investivation* **54.1,** (1974).

61. Yokoyama, T. & Farhi, L. E. Study of ventilation-perfusion ratio distribution in the anesthetized dog by multiple inert gas washout. SAM-TR-70-5. *Resp. Physiol.* **3.2,** 166–176 (1970).

62. Suki, B., Ito, S., Stamenović, D., Lutchen, K. R. & Ingenito, E. P. Biomechanics of the lung parenchyma: critical roles of collagen and mechanical forces. *J. Appl. Physiol.* **98,** (2005).

63. Wells, R. G. Tissue mechanics and fibrosis. *Biochim. Biophys. Acta - Mol. Basis Dis.* **1832,** 884–890 (2013).

64. Medlar, E. & Sasano, K. A study of pathology of experimental tuberculosis. *Am. Rev. Tuberc.* **34,** 456 (1936).

65. Hulnick, D. H., Naidich, D. P. & McCauley, D. I. Pleural tuberculosis evaluated by computed tomography. *Radiology* **149,** 759–765 (1983).

66. Sweany, H. C. & Seiler, H. H. The Pathology and Bacteriology of Resected Lesions in Pulmonary Tuberculosis. *Dis. Chest* **29,** 119–152 (1956).

67. Tsokos, M. *et al.* Pathology of fatal traumatic and nontraumatic clostridial gas gangrene: a histopathological, immunohistochemical, and ultrastructural study of six autopsy cases. *Int. J. Legal Med.* **122,** 35–41 (2008).

68. Jepson, P. D. *et al.* Gas-bubble lesions in stranded cetaceans. *Nature* **425,** 575–576 (2003).

69. Speare, D. J. Histopathology and ultrastructure of ocular lesions associated with gas bubble disease in salmonids. *J. Comp. Pathol.* **103,** 421–432 (1990).

70. Gill, S. E. & Parks, W. C. Metalloproteinases and their inhibitors: regulators of wound healing. *Int. J. Biochem. Cell Biol.* **40,** 1334–47 (2008).

71. Dannenberg, A. M. Liquefaction and cavity formation in pulmonary TB: a simple method in rabbit skin to test inhibitors. *Tuberculosis (Edinb).* **89,** 243–7 (2009).

72. Prideaux, B. *et al.* The association between sterilizing activity and drug distribution into tuberculosis lesions. *Nat. Med.* **21,** 1223–1227 (2015).

73. Lerner, T. R. *et al.* Mycobacterium tuberculosis replicates within necrotic human macrophages. *J. Cell Biol.* **216,** 583–594 (2017).

74. Kaczmarek, A., Vandenabeele, P. & Krysko, D. V. Necroptosis: the release of damage-associated molecular patterns and its physiological relevance. *Immunity* **38,** 209–23 (2013).

75. Ernst, J. D. The immunological life cycle of tuberculosis. *Nat. Rev. Immunol.* **12,** 581–591 (2012).

76. Roca, F. J. & Ramakrishnan, L. TNF dually mediates resistance and susceptibility to mycobacteria via mitochondrial reactive oxygen species. *Cell* **153,** 521–34 (2013).

77. Zhao, X. *et al.* Bcl-xL mediates RIPK3-dependent necrosis in M. tuberculosis-infected macrophages. *Mucosal Immunol.* (2017).

78. Butler, R. E. *et al.* Susceptibility of M. tuberculosis -infected host cells to phospho-MLKL driven necroptosis is dependent on cell type and presence of TNFα. *Virulence* **5594,** 7-17 (2017).

79. Pajuelo, D. *et al.* NAD+Depletion Triggers Macrophage Necroptosis, a Cell Death Pathway Exploited by Mycobacterium tuberculosis. *Cell Rep.* **24,** 429–440 (2018).

80. Chen, M., Gan, H. & Remold, H. G. A mechanism of virulence: virulent Mycobacterium tuberculosis strain H37Rv, but not attenuated H37Ra, causes significant mitochondrial inner membrane disruption in macrophages leading to necrosis. *J. Immunol.* **176,** 3707–16 (2006).

81. Mootoo, A., Stylianou, E., Arias, M. A. & Reljic, R. TNF- in Tuberculosis : A Cytokine with a Split Personality. *Inflamm. Allergy - Drug Targets* **8,** 53–62 (2009).

82. Keane, J. *et al.* Tuberculosis Associated with Infliximab, a Tumor Necrosis Factor α–Neutralizing Agent. *N. Engl. J. Med.* **345,** 1098–1104 (2001).

83. Bruns, H. *et al.* Anti-TNF immunotherapy reduces CD8+ T cell-mediated antimicrobial activity against Mycobacterium tuberculosis in humans. *J. Clin. Invest.* **119,** 1167–77 (2009).

84. Berghe, T. Vanden, Linkermann, A., Jouan-Lanhouet, S., Walczak, H. & Vandenabeele, P. Regulated necrosis: the expanding network of non-apoptotic cell death pathways. *Nat. Rev. Mol. Cell Biol.* **15,** 135–147 (2014).

85. de Almagro, M. C. & Vucic, D. Necroptosis: Pathway diversity and characteristics. *Semin. Cell Dev. Biol.* **39,** 56–62 (2015).

86. Dufour, F. *et al.* The ribonucleotide reductase R1 subunits of herpes simplex virus types 1 and 2 protect cells against TNFα- and FasL-induced apoptosis by interacting with caspase-8. *Apoptosis* **16,** 256–271 (2011).

87. González-Juarbe, N. *et al.* Pore-Forming Toxins Induce Macrophage Necroptosis during Acute Bacterial Pneumonia. *PLoS Pathog.* **11,** e1005337 (2015).

88. Vandenabeele, P., Galluzzi, L., Vanden Berghe, T. & Kroemer, G. Molecular

mechanisms of necroptosis: an ordered cellular explosion. *Nat. Rev. Mol. Cell Biol.* **11,** 700–714 (2010).

89. Vanden Berghe, T., Hassannia, B. & Vandenabeele, P. An outline of necrosome triggers. *Cell. Mol. Life Sci.* **73,** 2137–2152 (2016).

90. Danelishvili, L., Yamazaki, Y., Selker, J. & Bermudez, L. E. Secreted Mycobacterium tuberculosis Rv3654c and Rv3655c proteins participate in the suppression of macrophage apoptosis. *PLoS One* **5,** e10474 (2010).

91. Kramnik, I. & Beamer, G. Mouse models of human TB pathology: roles in the analysis of necrosis and the development of host-directed therapies. *Semin. Immunopathol.* **38,** 221–237 (2016).

92. Christofferson, D. E., Li, Y. & Yuan, J. Control of Life-or-Death Decisions by RIP1 Kinase. *Annu. Rev. Physiol.* **76,** 129–150 (2014).

93. Hussain, M., Zimmermann, V., van Wijk, S. J. L. & Fulda, S. Mouse lung fibroblasts are highly susceptible to necroptosis in a reactive oxygen species-dependent manner. *Biochem. Pharmacol.* (2018).

94. Kopalli, S. R., Kang, T.-B. & Koppula, S. Necroptosis inhibitors as therapeutic targets in inflammation mediated disorders - A review of the current literature and patents. *Expert Opin. Ther. Pat.* **3776,** 1239-1256 (2016).

95. Kramnik, I., Demant, P. & Bloom, B. B. Susceptibility to tuberculosis as a complex genetic trait: analysis using recombinant congenic strains of mice. *Novartis Found. Symp.* **217,** 120-31; discussion 132–7 (1998).

96. Skerry, C., Harper, J., Klunk, M., Bishai, W. R. & Jain, S. K. Adjunctive TNF inhibition with standard treatment enhances bacterial clearance in a murine model of necrotic TB Granulomas. *PLoS One* **7,** 1–7 (2012).

97. Ihms, E. A., Urbanowski, M. E. & Bishai, W. R. Diverse Cavity Types and Evidence that Mechanical Action on the Necrotic Granuloma Drives Tuberculous Cavitation. *Am. J. Pathol.* **188,** 1666–1675 (2018).

98. Moriwaki, K. & Chan, F. K. M. Necroptosis-independent signaling by the RIP kinases in inflammation. *Cell. Mol. Life Sci.* **73,** 2325–2334 (2016).

99. Stutz, M. D. *et al.* Necroptotic signaling is primed in Mycobacterium tuberculosis-infected macrophages, but its pathophysiological consequence in disease is restricted. *Cell Death Differ.* 1–15 (2017).

100. Amaral, E. P. *et al.* A major role for ferroptosis in *Mycobacterium tuberculosis* – induced cell death and tissue necrosis. *J. Exp. Med.* **216**, 556-570 (2019).

101. Ramos-Kichik, V. *et al.* Neutrophil extracellular traps are induced by Mycobacterium tuberculosis. *Tuberculosis* **89,** 29–37 (2009).

102. Mohareer, K., Asalla, S. & Banerjee, S. Cell death at the cross roads of host-pathogen interaction in Mycobacterium tuberculosis infection. *Tuberculosis* **113,**

99–121 (2018).

103. Berger, S. B. *et al.* Cutting Edge: RIP1 Kinase Activity Is Dispensable for Normal Development but Is a Key Regulator of Inflammation in SHARPIN-Deficient Mice. *J. Immunol.* **192,** 5476–5480 (2014).

Biography

Elizabeth A. Ihms was born in 1983 in the USA.

Elizabeth started her undergraduate work at Malone University in her hometown of Canton Ohio, before transferring first to Indiana Wesleyan University in Marion Indiana, and then to Texas A&M University, College Station, where she matriculated in 2006 with an undergraduate degree in Biology *cum laude* with an emphasis in microbiology.

After several years working in bacterial diagnostic laboratories at both Texas A&M and The Ohio State University, Elizabeth was accepted into The Ohio State University College of Veterinary Medicine, receiving her Doctorate of Veterinary Medicine *summa cum laude* in 2014.

In 2014, Elizabeth began residency in the Johns Hopkins University's Department of Molecular and Comparative Pathobiology program, receiving her Diplomate of the American College of Veterinary Pathology (DACVP) board certification in 2017. In 2015, Elizabeth began her PhD at Johns Hopkins University school of medicine in William Bishai's laboratory.